ELSEVIER

Journal of Structural Geology 28 (2006) 200–219

JOURNAL OF STRUCTURAL GEOLOGY

www.elsevier.com/locate/jsg

Application of trishear fault-propagation folding to active reverse faults: examples from the Dalong Fault, Gansu Province, NW China

Ryan D. Gold [a], Eric Cowgill [a,*], Xiao-Feng Wang [b], Xuan-Hua Chen [b]

[a] *Department of Geology, University of California, Davis, Davis, CA 95616, USA*
[b] *Institute of Geomechanics, Chinese Academy of Geological Sciences, Beijing, P.R. China*

Received 3 June 2005; received in revised form 18 October 2005; accepted 18 October 2005
Available online 5 December 2005

Abstract

Determining accurate fault slip rates at 1 ka to 1 Ma timescales requires well-constrained palinspastic reconstructions of dateable geomorphic and/or geologic markers. Although general kinematic models have been developed to simultaneously reconstruct both bedrock (e.g. bedding and fault attitudes) and neotectonic markers (e.g. strath terraces) along active strike-slip and thrust faults, it is not clear if these models can also account for deformation along steeply dipping ($>45°$) reverse faults. To address this problem, we have investigated the active, $\sim 50°$ dipping, Dalong reverse fault system. This $\sim$40-km-long fault system forms part of the Aksai restraining stepover along the active, left-slip Altyn Tagh Fault in northwestern China. Our geometric and kinematic analyses show that conventional fault-bend fold models cannot satisfy the steeply-dipping fault geometry we observe in the bedrock record. Likewise, standard fault-propagation fold models fail to match our measurements of a set of fluvial terraces. However, by expanding the trishear model of fault-propagation folding to track both bedrock and neotectonic markers, we are able to match both sets of records. In particular, we have developed trishear kinematic models for two sites (Liuchenzi and Qingyazi) using the numerical modeling program, Fault/Fold v.5.0. This work indicates that an important implication of active trishear fault-propagation folding is that terrace deformation extends for over 1 km on either side of the fault trace. Thus, to accurately measure the total magnitude of vertical separation between matching terraces in the hanging wall and footwall, terrace profiles across active reverse faults must extend 1–2 km on either side of this zone of deformation.

Keywords: Trishear; Reverse faults; Fault-propagation folds; Transect data; Neotectonics; Restraining bends

1. Introduction

Measuring accurate Quaternary slip rates on active fault systems is central to determining both seismic recurrence intervals (e.g. Xu and Deng, 1996; Yeats and Prentice, 1996) and if slip rates vary at decadal to millennial timescales (Friedrich et al., 2003; Weldon et al., 2004; Chevalier et al., 2005). Significant work has focused on determining Quaternary slip rates along strike-slip fault systems like the San Andreas Fault in California (e.g. Weldon and Sieh, 1985; Matmon et al., 2005) and the Altyn Tagh Fault in NW China (e.g. Chen et al., 2000; Washburn et al., 2001; Meriaux et al., 2004), as well as shallowly dipping thrust fault systems like the Himalayan Main Frontal Thrust (e.g. Lavé and Avouac, 2000) and thrusts within the Tien Shan (e.g. Thompson et al., 2002). However, less work has focused on determining slip-rates along active reverse fault systems ($>45°$ dip). These steeply dipping fault systems, particularly those associated with transpression across restraining stepovers along major strike-slip fault systems, have increasingly been recognized as sites of particular seismic hazard (e.g. Rubin et al., 1998; Anderson et al., 2003; Manaker et al., 2005), and thus merit attention.

Two elements are essential for accurate slip-rate determinations: (1) a precise palinspastic reconstruction of deformed markers for which (2) accurate age information can be obtained. An important, and often overlooked, aspect of the first element is knowledge of the subsurface fault geometry. In general, previous work varies in the extent to which both bedrock (e.g. bedding, foliation, or fault attitudes) and neotectonic (e.g. topographic profiles of deformed strath terraces) data have been combined to

* Corresponding author. Tel.: +1 530 754 6574; fax: +1 530 752 0951.
E-mail address: cowgill@geology.ucdavis.edu (E. Cowgill).

0191-8141/$ - see front matter © 2006 Elsevier Ltd. All rights reserved.
doi:10.1016/j.jsg.2005.10.006

constrain neotectonic reconstructions. Three general approaches have been used.

The first type of study relies solely on the neotectonic record. For example, one method combines the vertical separation of a displaced geomorphic feature with its surface-exposure age to calculate the rate of vertical uplift of the hanging wall relative to the footwall (Ritz et al., 2003). Because this type of analysis ignores subsurface fault geometry, it can only be used to derive the vertical component of the fault slip rate. Additionally, if only a single strain marker is considered, this technique yields a minimum slip rate because of the possibility that the surface formed long before it was ruptured to form the fault scarp. An alternative, but still purely neotectonic, approach uses an elastic dislocation model to generate synthetic terrace profiles that are compared with measured terrace profiles to constrain both the fault geometry and its kinematic evolution (Benedetti et al., 2000; Vannoli et al., 2004). However, this method does not further test the kinematic model against observed bedrock structural geometries.

The second class of slip-rate studies partially integrates neotectonic and bedrock data. In these investigations, local bedding and fault attitudes in the bedrock record are used to construct balanced cross-sections, which constrain subsurface fault geometry; then, surface dating methods are applied to the young river deposits to constrain fault slip-rates (e.g. Meyer et al., 1998; Van der Woerd et al., 2001). Although this method better constrains subsurface fault geometry, it does not geometrically or kinematically link bedrock deformation to recent folding and faulting of river deposits. Thus, although the partial integration of the bedrock and neotectonic datasets yields more well-constrained slip-rates, its reliance on an unproven tie between the two geologic records prevents definitive slip-rate calculations.

The third group of studies fully integrates bedrock and neotectonic data, but has only been applied to shallowly dipping faults. In a study of active folding along the Main Frontal Thrust in the sub-Himalaya, Lavé and Avouac (2000) applied fault-bend fold theory (Suppe, 1983) to bedrock measurements to generate synthetic terraces, which they then compared with field measurements of fluvial terrace surfaces. Thompson et al. (2002) followed a similar approach in the Tien Shan. Both studies yielded a high degree of correlation between synthetic and measured terrace profiles. Through geometric and kinematic modeling of both the bedrock and neotectonic records, this method provides robust constraints on slip rates on shallowly

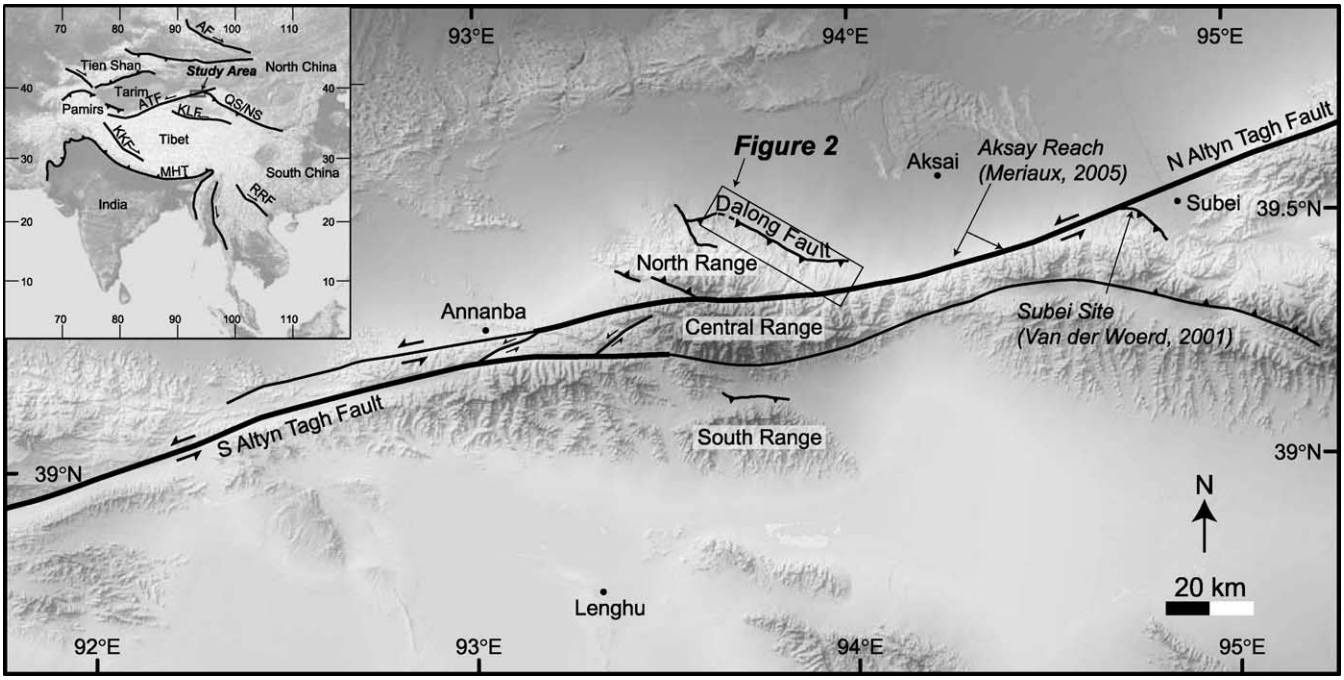

Fig. 1. Map of active faults showing the tectonic setting of the Aksai restraining stepover along the Altyn Tagh Fault. The restraining stepover is defined by the overlap of two active strands of the Altyn Tagh Fault, a southern strand in the west and a northern strand in the east. The locations of these strands were compiled from our structural mapping and image interpretation as well as previous work (Chinese State Bureau of Seismology, 1992; Meriaux et al., 2005). West of 93°E, the southern strand is the primary trace, as indicated by the bold line, whereas east of 93.5°E, the primary trace is the northern strand. These two strands of the Altyn Tagh Fault divide the stepover into northern, central, and southern ranges. The flank of northern range is defined by the south-dipping Dalong Fault. The fault traces are overlain on a hillshaded map produced from SRTM90 topographic data (ftp://edcsgs9.cr.usgs.gov/pub/data/srtm/). The box around the Dalong Fault outlines the area of the geologic map shown in Fig. 2. The inset map shows simplified Quaternary faults of the Indo-Asia collision (compiled from Peltzer and Tapponnier, 1988; Yin and Harrison, 2000; Ritz et al., 2003): ATF, Altyn Tagh Fault; AF, Altai Fault; KKF, Karakorum Fault; RRF, Red River Fault; MHT, Main Himalayan Thrust; KLF, Kunlun Fault; QS/NS, Qilian Shan/Nan Shan. The fault traces are overlain on a hillshaded map derived from the SRTM30 digital elevation model (ftp://topex.ucsd.edu/pub/srtm30_plus/).

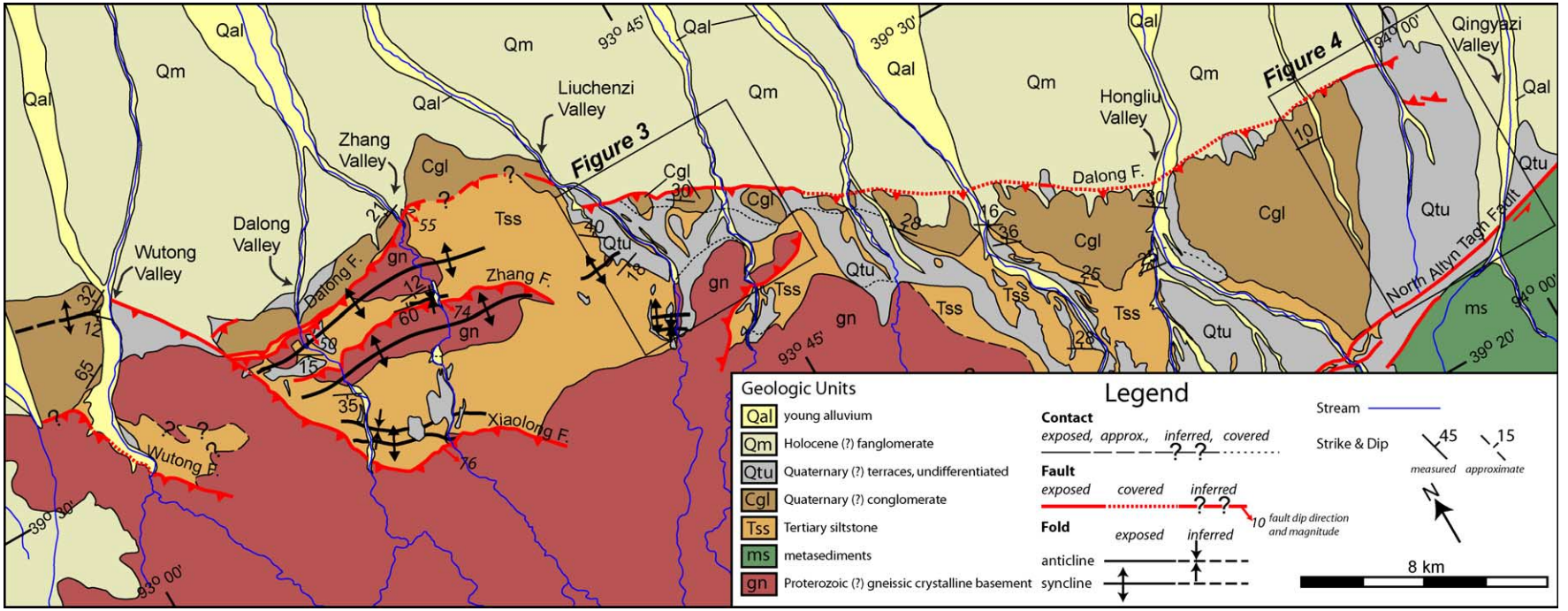

Fig. 2. Simplified geologic map of the Dalong fault system based primarily on our 1:100,000 structural mapping with additional input from previous work (GBG, 1977; Wang, 1997). The fault system extends from the Dalong Valley in the west to the Qingyazi Valley in the east. The fault system appears to reflect greater total shortening in the west than in the east (Cowgill et al., 2004a). The east end of the system is defined by a single active fault trace and a broad, hanging-wall anticline, which deforms the sedimentary cover. In contrast, at the west end of the system, three south-dipping reverse faults expose deeper structural levels by placing north-directed, hanging-wall anticlines cored by gneiss over the sedimentary cover. Boxes outline detailed study locations at Liuchenzi (Fig. 3) and Qingyazi (Fig. 4). From oldest to youngest, the geologic units are: gn, Archean gneiss of northern range; ms, metasediments of the central range; Tss, Tertiary siltstone; Cgl, Quaternary (?) conglomerate; Qtu, old Quaternary terrace, undifferentiated; Qm, fanglomerate; Qal, active alluvial deposit. See the online article for the colour version of this figure.

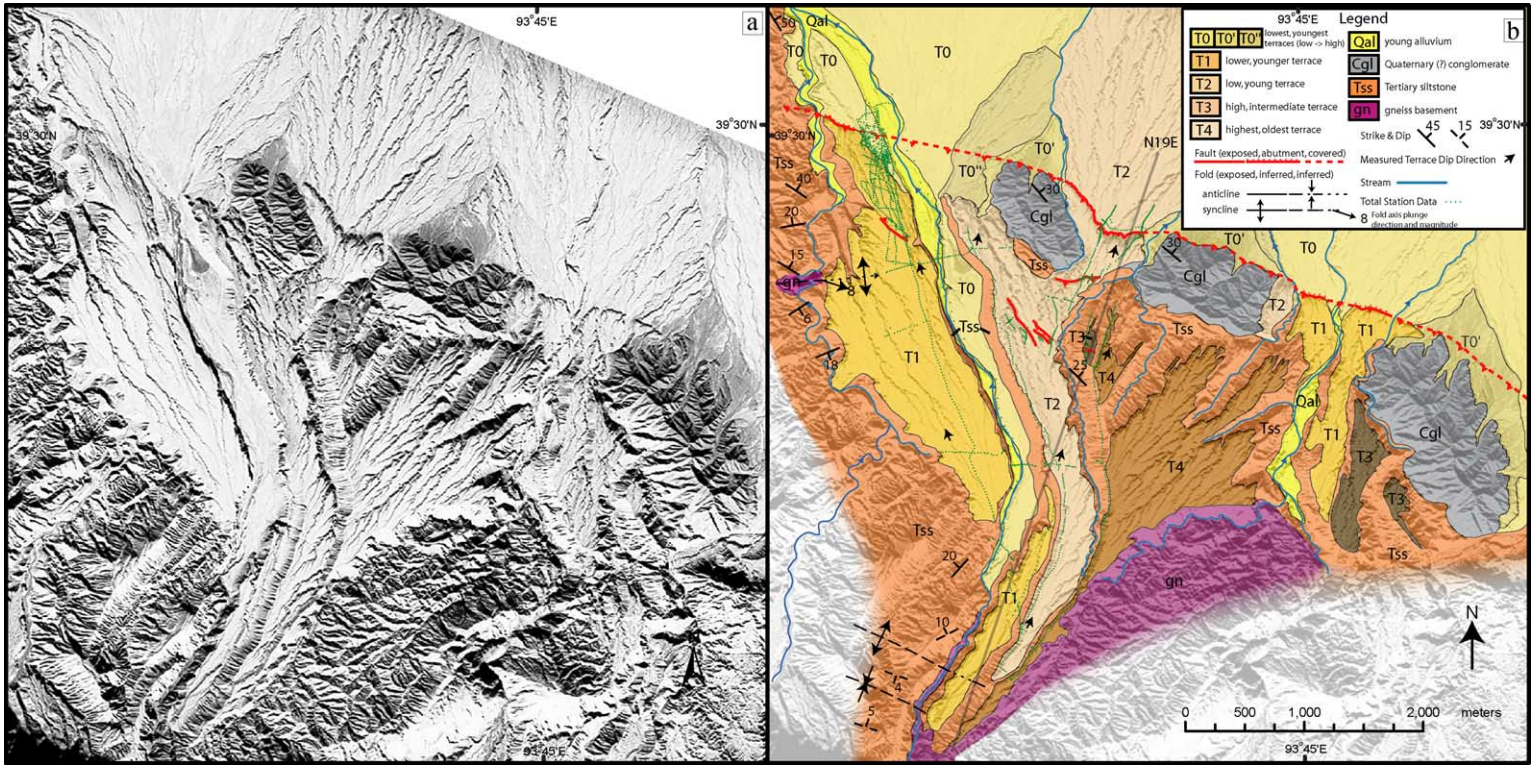

Fig. 3. Liuchenzi site. (a) Section of uninterpreted Corona image DS1105-1071DA086. (b) Neotectonic map of Liuchenzi with geology, total station data (green dots), and line of cross-section. Total station data show $\pm$30 m inaccuracies in registration relative to the underlying mapping due to errors in the orthorectification of the underlying base Corona image caused by the lack of sensor information for this formerly classified instrument. Red fault traces with flanking dots indicate the locations where a fault scarp both cuts an older unit, but is also capped by a younger deposit. The dots lie on the younger unit.

dipping fault systems. However, it remains to be determined if these kinematic models can also be extended to simultaneously explain both the bedrock and neotectonic deformation along steeply dipping (>45°), basement-involved faults.

To address this problem, we investigated the active Dalong Fault in NW China. This reverse fault system deforms crystalline basement and a thin cover of late Cenozoic terrestrial clastic sediments, which here is collectively referred to as the 'bedrock' record, and a younger suite of fluvial strath terraces, which is here called the 'neotectonic' record. We begin with a review of the tectonic setting of the Dalong system, and then summarize field observations derived from our structural and neotectonic mapping, done at 1:100,000 and 1:54,000 scales, respectively. To form a single set of geometric constraints, we then integrate key bedding and fault attitudes with drainage-parallel topographic profiles measured across the faulted and folded fluvial terrace systems. We use these constraints to develop a geometric and kinematic model of the Dalong fault system. We find that fault-bend and kink-band fault-propagation models fail to satisfy the integrated bedrock and neotectonic data. As a result, we have extended the trishear model of fault-related folding to active reverse faults, and find that, to a first-order, this model matches our bedrock and neotectonic data along the Dalong Fault.

2. Geologic setting

2.1. Aksai stepover

The active, left-slip Altyn Tagh Fault strikes 070° for over 1200 km along the northwestern margin of the Tibetan Plateau (Fig. 1 inset), and is thought to help accommodate north–south Indo-Asian convergence through the east-directed, lateral extrusion of Tibet (Molnar and Tapponnier, 1975, 1978; Tapponnier and Molnar, 1977). Between 85°E and 95°E, the fault is punctuated by four, right-stepping restraining double bends (Cowgill et al., 2004b). Local convergence within these bends has produced 50–100-km-long mountain ranges that are centered on each bend (Cowgill et al., 2004b). The Aksai restraining stepover is the easternmost of these bends. At this locality, the Altyn Tagh Fault comprises two main active strands that divide the bend into three separate ranges (Fig. 1). The northern and southern ranges flank the restraining bend to the north and south, respectively, and are each ~70 km long (east–west) and ~25 km wide (north–south). In contrast to the 070° strike of the Altyn Tagh Fault outside the bend, geomorphically less well-expressed segments of the fault within the stepover strike 085–095°.

Previous investigations of the Aksai stepover have focused on characterization of the active Altyn Tagh Fault traces (Chinese State Bureau of Seismology, 1992), bedrock shortening in the northern range (Wang, 1997), total displacement along the fault based on sedimentary basin reconstructions (Wang, 1997), and thermochronologic documentation of Mesozoic ductile deformation (Delville et al., 2001; Jolivet et al., 2001).

2.2. Northern Aksai Range

The northern Aksai Range lies to the north of the restraining stepover and is bounded to the south by the northern strand of the Altyn Tagh Fault and to the north by the Dalong reverse fault (Fig. 1). The northern Altyn Tagh Fault strikes ~90° in the central portion of the stepover and is geomorphically expressed as an east–west-trending valley, but shows limited evidence of recent surface rupture. The active Dalong reverse fault system strikes northwest–southeast for ~40 km (Fig. 2), and likely results from transpression within the Aksai stepover (Cowgill et al., 2004a).

3. Geology of the Dalong Fault

3.1. Bedrock observations

Our investigation of the Dalong fault system provides bedrock structural observations that constrain geometric models of the Dalong Fault. This active, south-dipping reverse fault generally separates a bajada surface with no bedrock exposure in the footwall to the north, from exposures of gneiss, sandstone, and conglomerate in the hanging wall to the south (Fig. 2). As our simplified geologic map in Fig. 2 indicates, structural style varies systematically along strike, apparently reflecting larger magnitudes of total shortening in the west than in the east (Cowgill et al., 2004a). The east end of the system is defined by a single active fault trace and a broad, hanging-wall anticline that deforms sedimentary cover deposits. In contrast, the west end of the system comprises three, south-dipping reverse faults that expose deeper structural levels by placing north-directed, hanging-wall anticlines cored by gneiss over the sedimentary cover units (Fig. 2).

Based on our geologic mapping and previous studies of the northern Aksai range (GBG, 1977; Wang, 1997; Cowgill et al., 2004a), we define four main geologic units (Fig. 2). Stratigraphically lowest and oldest is Archean (?) crystalline basement (gn), which cores the range. The base of this unit is not exposed in the field area and, thus, we could not constrain its thickness. A package of orange siltstone and interbedded sandstone and conglomerate (Tss) unconformably overlies the basement. We estimated the thickness of Tss (~550 m) at the Liuchenzi Valley (Fig. 3) by measuring the vertical distance between the basal and upper contacts of this unit and accounting for bedding orientation. These rocks were tentatively correlated by Wang (1997) with the Xishuigou redbed sequence, ~100 km east, near Subei, which is thought to be

10–20 Ma (Gilder et al., 2001; Yin et al., 2002; Wang et al., 2003). Unconformably overlying the redbed unit is a brown and gray, cobble-to-boulder conglomerate (Cgl) with a matrix of red silt and minor sand. We were unable to constrain the total thickness of the Cgl unit. An analogous unit on the GBG (1977) map is reported to be ~320 m thick. Wang (1997) assigns this unit an early Pleistocene age by correlating with other dated rocks in region. The youngest geologic units in the area are late Quaternary flights of incised strath terraces, which are discussed in detail in Section 3.2 below.

At the eastern section of the Dalong fault system, near the Qingyazi drainage (Figs. 2 and 4), the active trace of the fault strikes ~275° and separates a gently deformed package of uplifted Cgl in the hanging wall from a younger alluvial deposits (Qm) in the footwall (Fig. 2). Cgl is the only exposed bedrock in this area and generally dips <15° north (Fig. 4). We assumed that the Cgl unit was deposited on a slope dipping 5°, which is consistent with the modern drainage gradient of 4°. Locally, streams do not expose deeper structural levels because the Cgl unit and the modern drainage have similar dips. We inferred the underlying stratigraphy by using stratigraphic thicknesses calculated at the Liuchenzi site (Figs. 2 and 3). No cross-sectional exposures of the Dalong Fault were found at Qingyazi.

Farther west, between the Hongliu and Liuchenzi Valleys (Fig. 2), the active trace of the Dalong Fault strikes ~295°. The linear map trace of the fault between the Hongliu and Liuchenzi Valleys (Fig. 2) indicates that the fault is generally steeply dipping. At the western portion of this reach, at the Liuchenzi site (Figs. 2 and 3), there is a northward younging of bedrock units in the hanging wall. In the south (Fig. 3b), a ridge of gneiss is overlain by Tss, which dips shallowly north by 5–20°. Approximately 3 km to the northwest of the gneiss ridge, along the western edge of Fig. 3b, a small knob of crystalline basement is unconformably capped by Tss beds, and is exposed in the core of an anticline. Beds dip 15–20°N and 6–18°S on the north and south limbs of the anticline, respectively (Fig. 3). We calculated the orientation of the fold axis, and then projected the hinge line defined by the gn-Tss unconformity down plunge and into the N19E plane of section (Fig. 3) to

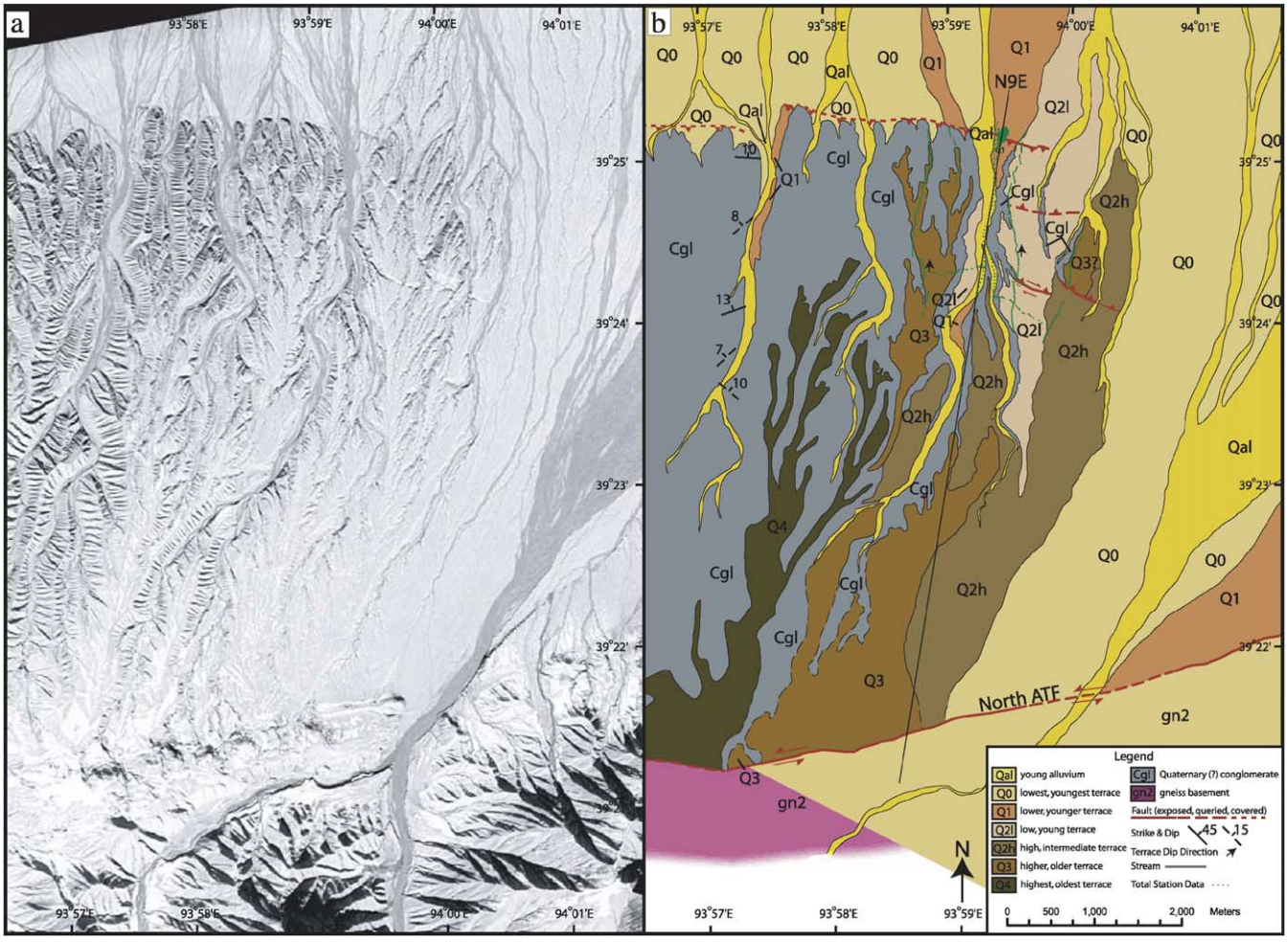

Fig. 4. Qingyazi site. (a) Portion of uninterpreted Corona image DS1105-1071DA086. (b) Neotectonic map of Qingyazi site geology. See caption to Fig. 3b for additional information regarding symbols. See the online article for the colour version of this figure.

obtain a key constraint for the geometric models developed in Section 4 below. To make this calculation, we plotted both limbs of the fold on a stereoplot and found that the limbs approximate a cylindrical best-fit (Fig. 5d). The fold axis we derived trends 110° and plunges 8°. North of the hanging-wall anticline, but south of the Dalong Fault scarp, the Tss unit is overlain by Cgl, which together dip moderately (30–40°) northward. Cross-sectional exposures of the Dalong Fault were not observed at Liuchenzi site.

At the western extent of the Dalong fault system, the Dalong, Zhang, and Xiaolong Faults are exposed in the Zhang and Dalong Valleys (Fig. 2). Each south-dipping fault places a hanging-wall anticline cored by crystalline basement (gn) over the sedimentary cover (Tss and Cgl). The gn exposures above the Dalong and Zhang faults are <2 km thick, perpendicular to the fault. Exposures in the Zhang and Dalong Valleys reveal steeply dipping faults (Figs. 2 and 5c and d). A compilation of fault orientations measured along the Dalong Fault yields an average dip of $\sim 51°$ (Fig. 5d). Although these faults were not observed to directly link to the east with the Dalong Fault in the Liuchenzi and Qingyazi Valleys, we infer that this reach of the fault also dips $\sim 50°$, based on the linear map trace of the active fault between the Hongliu and Liuchenzi valleys.

In summary, the bedrock geology along the Dalong Fault yields four key constraints for the geometric and kinematic modeling below: (1) the orientations of bedding within the Tss and Cgl units, (2) the locations and orientations of the gn–Tss and Tss–Cgl contacts, (3) the presence of a gently east-plunging anticline that is cored by gneiss at a shallow structural level in the plane of the cross-section, and (4) a steeply dipping ($>45°$) Dalong Fault.

3.2. Neotectonic observations

North-flowing drainages have incised valleys and emplaced suites of terrace deposits in the northern Aksai Range. Our neotectonic observations of these strath terraces near the Dalong fault system consisted of (1) mapping the trace of the fault and the distribution of fluvial terrace deposits and (2) surveying topographic profiles across the terrace surfaces.

3.2.1. Neotectonic mapping

We conducted $\sim$1:54,000-scale, field-based neotectonic mapping to identify the distribution of fluvial strath terraces. To correlate terraces and determine their relative depositional timing, we used terrace elevations above the active drainage, the degree of incision, and the amount of loess cover on the terrace surfaces. Although terrace correlations within individual drainages were straightforward, the lack of along-strike continuation of the terraces prevented definitive correlation between drainages. Thus, we differentiate terraces in Liuchenzi (T) from those in Qingyazi (Q).

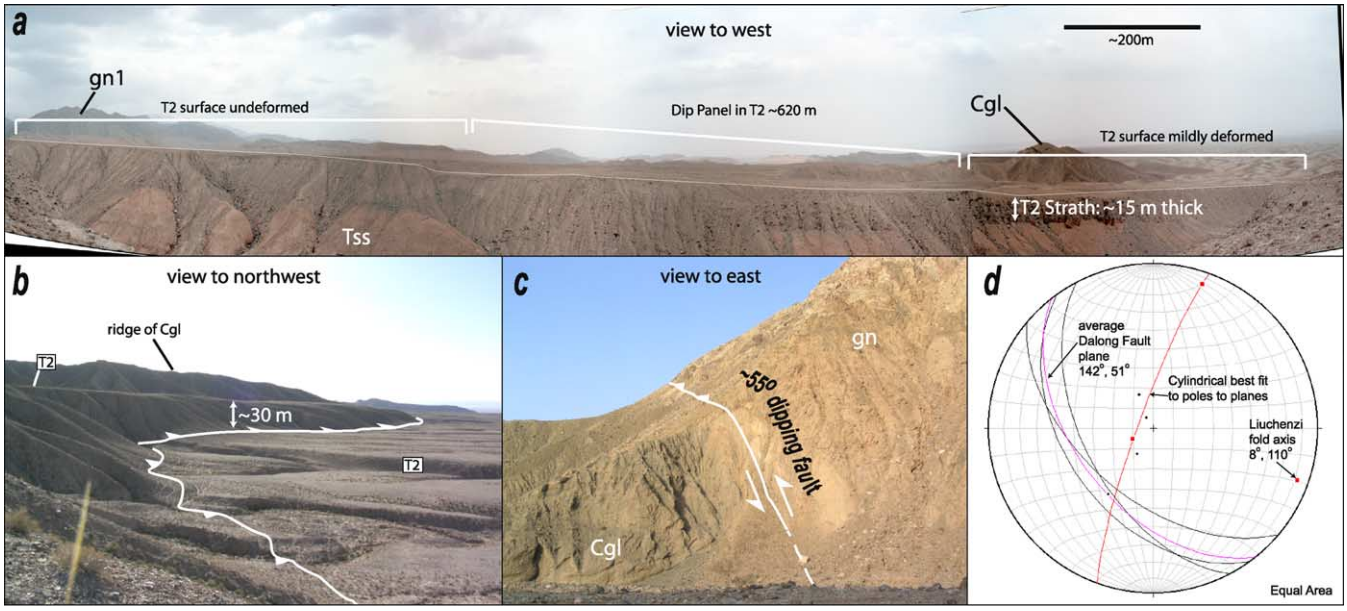

Fig. 5. Field observations of the Dalong Fault and hanging wall. (a) Photomosaic of the T2 strath terrace and underlying Tss unit at the Liuchenzi site. Thin white line delineates edge of terrace tread. For scale the terrace deposit is $\sim$15 m thick. The 620-m-long dip panel in the T2 surface places a key constraint on subsurface fault geometry, as discussed in the text. (b) Dalong Fault scarp east of Liuchenzi valley separates T2 surface with 30 m of vertical displacement. Photo was taken from the northwest corner of the middle of the three Cgl exposures shown on Fig. 3b, and shows the scarp where it crosses the line of section. (c) Photo of the $\sim$55° dipping Dalong Fault as exposed on the east wall of the Zhang Valley (Fig. 2). At this locality the fault places crystalline basement (gn) in the hanging wall over conglomerate (Cgl) to the north. (d) Equal area, lower hemisphere stereoplot of key structural measurements. Black great circles show measurements of the Dalong Fault in the Zhang and Dalong Valleys. Thick black great circle indicates the average fault plane, which dips 51°SW. Black dots indicate poles to bedding planes within the Tss unit as measured on opposite sides of an anticline that exposes gneiss in its core along the west edge of Fig. 3b. A cylindrical best fit to these poles indicates that the fold axis trends 110° and plunges 8° where it deforms the Tss/gn contact. See the online article for the colour version of this figure.

In our terrace-naming convention, numbers increase from youngest to oldest, such that T0 and Q0 are the youngest and T4 and Q4 are the oldest surfaces.

In the Liuchenzi area, a number of surfaces (T0, T0′, T0″, Qal) are still subject to active deposition/transport by the modern drainage network, especially in the hanging wall of the Dalong Fault (Fig. 3). Four other incised and deformed strath terraces (T1–T4) have been cut into the underlying Tss and gn units. The lowest/youngest abandoned terrace (T1) defines a broad surface on the west side of the valley, with the remaining three terraces (T2–T4) preserved on the east side of the valley (Fig. 3b). As Figs. 3b and 5b indicate, the Dalong Fault cuts the T2 surface but is capped by the T0 and T1 surfaces. Between the two central knobs of Cgl that straddle the line of section on Fig. 3b, the Dalong Fault cuts the T2 surface with an arcuate map trace. This may suggest that the Dalong Fault locally has a shallow dip. A series of back-thrusts and small grabens cut all terraces except for T0 within a kilometer south of the Dalong Fault. These secondary structures strike sub-parallel to the main fault.

The terrace deposits at Liuchenzi range from 10 to 20 m in thickness and are composed of sand, gravels, and small cobbles in a matrix of silty sand. In general, the degree of incision and loess cover both increase with terrace height above the modern drainage. In contrast, preservation of channel-and-bar topography and the size and concentration of surface clasts both decrease with terrace height. More detailed terrace descriptions are provided in the Appendix.

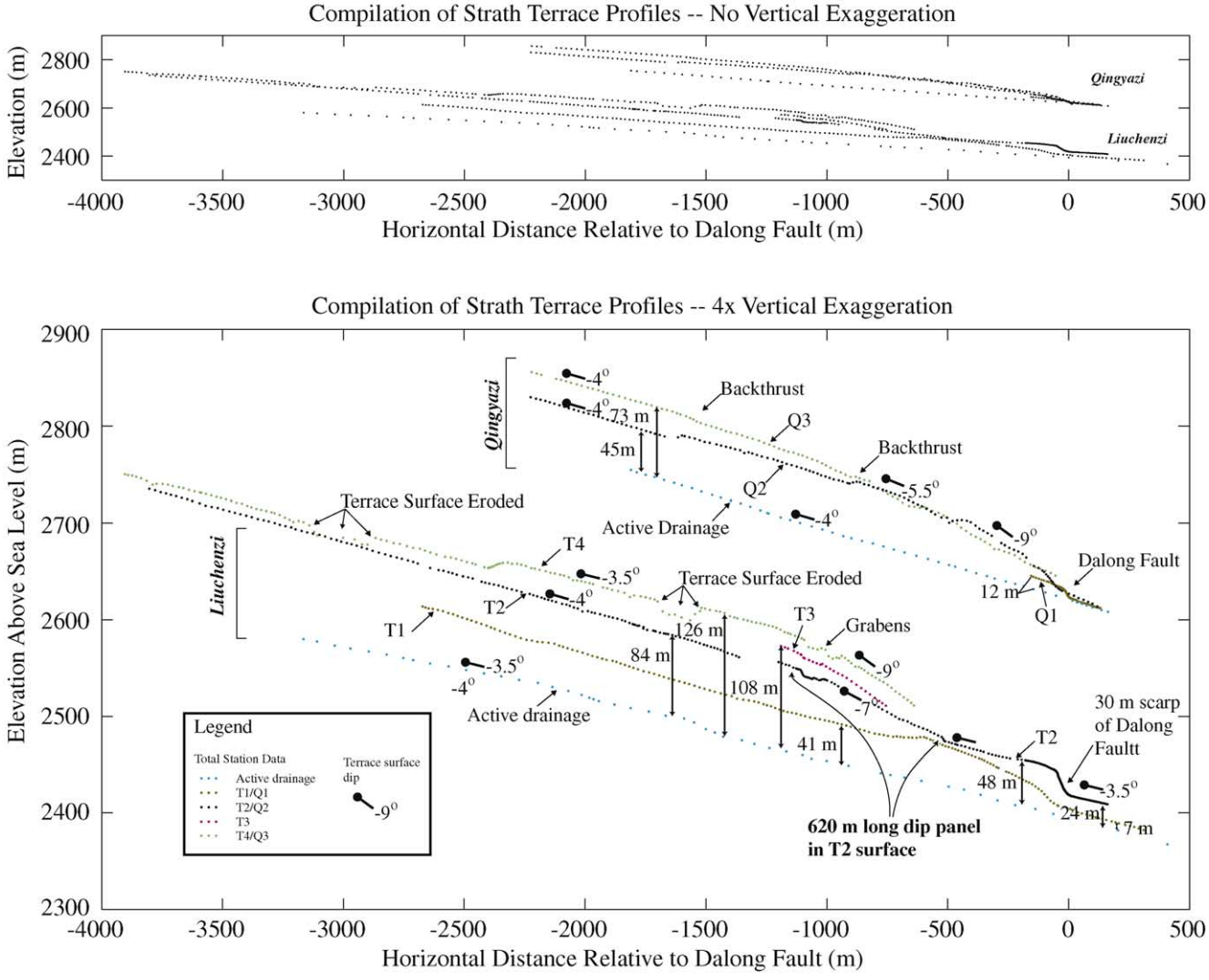

Fig. 6. Topographic profiles projected onto lines perpendicular to the Dalong Fault for the Liuchenzi and Qingyazi sites. (a) Plots of survey data shown with no vertical exaggeration. (b) Plots shown with 4× vertical exaggeration. Terrace heights measured above the modern drainage are indicated. Also, the magnitudes of terrace dips are reported as non-vertically exaggerated values (note: the dip ticks are steepened to dip 4× to match the vertical exaggeration of the figure). Point positions along individual profiles were measured relative to an arbitrary datum. The profile lengths and accuracy of the total station are such that relative positions of points within a given set of profiles are accurate to within 15 cm. The surveys were georeferenced to the map using control points that were measured using a handheld GPS unit. These GPS locations were also used to assign absolute elevations (relative to mean sea level) to each arbitrary datum. Thus, the absolute elevations of the topographic profiles are only known to ±40 m. See the online article for the colour version of this figure.

At Qingyazi (Figs. 2 and 4), there are four incised and deformed terraces (Q1–Q4), in addition to the active Q0 surface. These terraces systematically step upward from east to west. The Dalong Fault cuts the Q1 and Q2 surfaces, and a series of back-thrusts cut the Q2 terrace up to ~1.5 km south of the main trace. The thickness of the terrace deposits at Qingyazi is difficult to constrain because no clear contact was observed between the base of the terrace deposits and the top of the underlying Cgl conglomerate. A pit dug into Q1 reveals that this deposit is composed of poorly stratified gravel and cobbles in a silty sand matrix and is covered by >40 cm of loess. All of the terraces have more loess cover and a lower concentration of surface clasts than the terraces at Liuchenzi. As Fig. 4 indicates, within 1 km of the Dalong Fault, the Qingyazi terrace surfaces are discontinuous, heavily incised, and often preserved only along narrow ridges. To the south and farther upslope, the terrace units are more continuous and have smooth surfaces. The higher terraces (Q2–Q4) show a greater degree of incision and no preservation of channel-and-bar structure in comparison with the lower surfaces (Q0–Q1), which are less incised but show more surface roughness because of the partial preservation of channel-and-bar topography.

3.2.2. Quantitative terrace profiles

At both Liuchenzi and Qingyazi we surveyed topographic profiles along terraces transverse to the Dalong Fault and parallel to the active drainage. Measurements were made using a digital-recording theodolite-distance-meter (Leica TCR407power) and a PDA with FieldGenius XG 2.0 data collection software. Procedures and uncertainties with this method are discussed in general terms by Avouac (1993) and Thompson et al. (2002). Because the precision of the total station (7 s) and the length of profiles (<5 km) result in measurement errors that are less than 15 cm, natural surface roughness is larger than the measurement error.

At the Liuchenzi site, we measured profiles along the four incised terraces and the active drainage (Fig. 6). To use these measurements to constrain cross-sections of the Dalong Fault, we projected them onto a vertical plane that trends 019°, perpendicular to the local strike of the Dalong Fault. As Fig. 3b indicates, there are a number of localities where we measured secondary profiles that trend roughly orthogonal to the main survey line. We determined the local dip of the terrace surface at these localities by finding points of equal elevation on the crossing survey lines (Figs. 3b and 4b). As the surface dip arrows on Fig. 3b indicate, the terrace surfaces dip in the same direction as the line of section, thus to project the topographic data along the strike of the terrace surfaces we simply projected them along lines perpendicular to the line of the cross-section.

At the Liuchenzi site, from north to south, the projected topographic profiles indicate (1) a ~30-m-high fault scarp at the surface break of the Dalong Fault (Figs. 5b and 6), (2) a 620-m-wide (horizontal measurement) dip panel within which the T2–T4 terraces dip twice as much (7–9°) as they do to the north or south (3–4°) (Figs. 5a and 6b), (3) undeformed T2 and T4 terrace surfaces that extend south for over 2300 m (from profile position −1200 m to over −3500 m) (Fig. 5a), and (4) vertical distances between the active drainage and the terraces at distances >1 km south of the fault scarp of ~40 m for T1, ~85 m for T2, ~110 m for T3, and ~125 m for T4 (Fig. 6). Secondary observations include minor surface deformation (<3 m) including normal faults, and eroded portions of the terrace profiles.

At Qingyazi, we measured profiles across the Q2 and Q3 surfaces and the active drainage and projected the data onto a section trending 009° (Fig. 6). This orientation was selected because it is orthogonal to the local trend of the Dalong Fault scarp. In addition, there is a short profile of the Q1 surface that is cut by the Dalong Fault. The first-order observation of these profiles include (1) a northward increasing dip from 4.5 to 9° near the fault scarp, and (2) throws of ~50 m for Q2 and ~75 m for Q3. Second-order features include small (<3 m) back-thrust scarps.

4. Geometric and kinematic interpretation

4.1. Integration of datasets: method and assumptions

To integrate the bedrock and neotectonic data described above into a single set of geometric constraints, we projected all of the data onto vertical cross-section planes oriented perpendicular to the local strike of the Dalong Fault. We then generated a series of cross-sections that grossly satisfy these data but differ in terms of both assumed structural style and degree of fit to the data. To generate these kinematic models, we made several assumptions, which we discuss here.

The first assumption is that the ~27-km-long fault scarp observed between the Liuchenzi (Fig. 3b) and Qingyazi (Fig. 4b) sites is a break-out of the main Dalong Fault. As discussed by Allmendinger (1998) and others (Mitra, 1990; Suppe and Medwedeff, 1990) a break-out (also called a 'breakthrough') results when the fault associated with fault-propagation folding abandons the fold by cutting rapidly through the stratigraphic section. By assuming that the fault is a break-out, we were able to use the 30-m-vertical T2 scarp at Liuchenzi (Fig. 5b) to constrain vertical offset along the fault.

The second assumption is that each terrace surface represents an isochronously formed, and passively deformed, strain marker. While it has been shown that terrace surfaces can be strongly diachronous (Weldon (1986), as cited in Burbank and Anderson (2001)), we followed previous investigations by making the simplifying assumption that the entire surface of an individual strath terrace records an approximately isochronous period of deposition that is followed by abandonment and stream incision. The same assumption was made in analysis of

fluvial terraces along the Aksay and Tula (Tura) segments of the Altyn Tagh Fault (Meriaux et al., 2004, 2005), at the intersection of the Altyn Tagh Fault and the Tanghe Nan Shan (Van der Woerd et al., 2001), and in the Tien Shan (Avouac and Peltzer, 1993; Molnar et al., 1994; Thompson et al., 2002). By making this assumption, it follows that a permissible kinematic model of the Dalong Fault must provide a geologically-plausible sequence of terrace deposition, in addition to matching the bedrock geometric constraints.

The third assumption we made to evaluate the cross-sectional models is that the terraces (particularly the T2

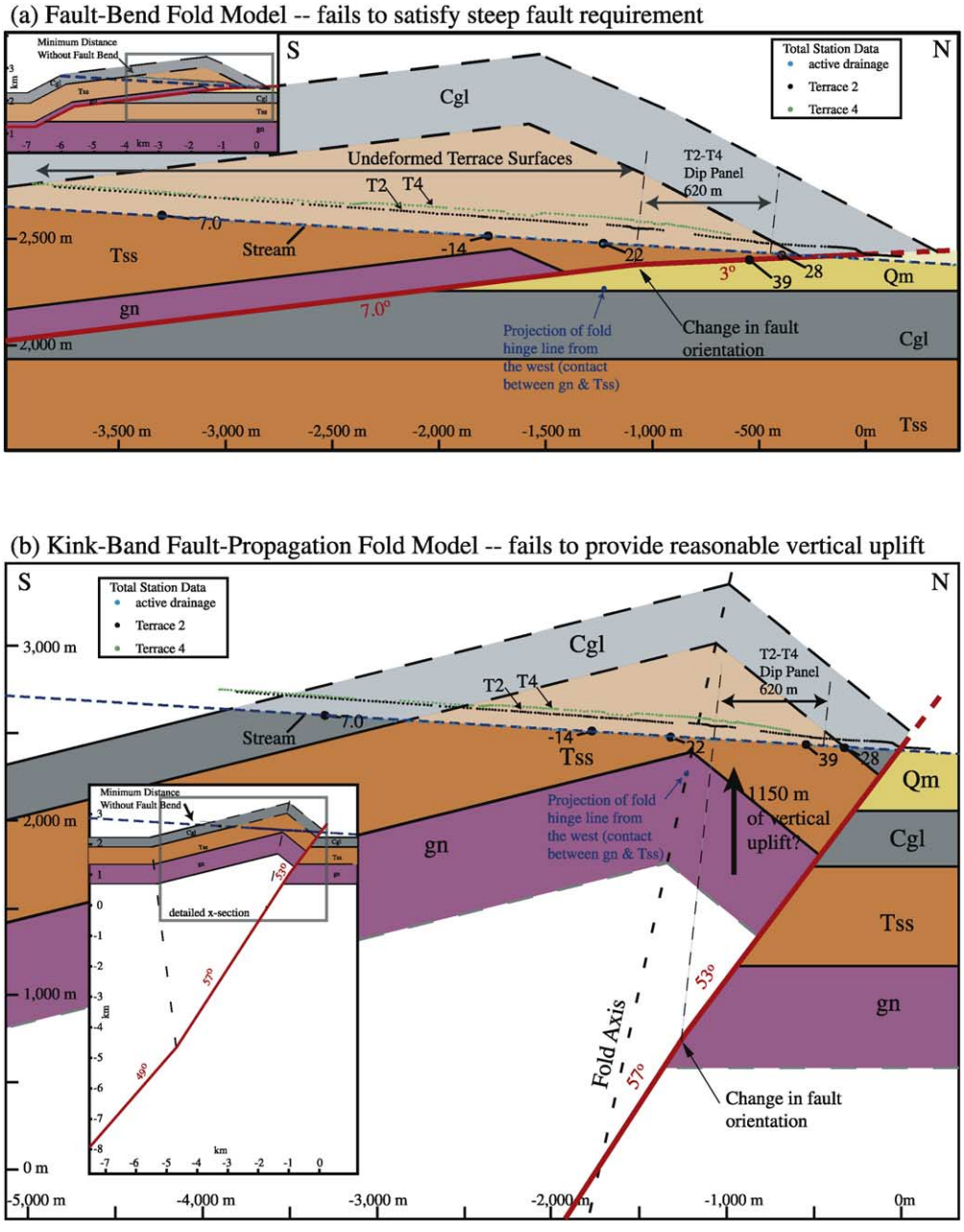

Fig. 7. Failed cross-sectional models of the Liuchenzi site. (a) Fault-bend-fold model. Inset shows whole model. Although this solution satisfies most of the neotectonic and bedrock data, it makes four unrealistic implications for the Dalong fault: (1) the Dalong fault dips $<10^{\circ}$ to at least 3.7 km south of the frontal scarp, in contrast to the observed $\sim 50^{\circ}$ dip in the Zhang and Dalong Valleys. (2) There is a $\sim$6.8-km-long sliver of basement that is only a few hundred meters thick, inconsistent with observed basement exposures in the Zhang and Dalong Valleys. (3) If T2 is $<$18.5 ka, then this solution implies an unreasonably high minimum horizontal shortening rate of at least 33 mm/yr. (4) The location of the fold axis along the gn–Tss contact lies $\sim$500 m from the position of this point as projected into the section from surface data. (b) Kink-band fault-propagation-fold model. Inset shows whole model. This solution satisfies the bedrock data, but it makes two unrealistic predictions. (1) It requires 1150 m of vertical separation to transport material 620 m in the horizontal direction and form the T2–T4 panel. This is inconsistent with both the 30-m-high fault scarp and the height of the T4 terrace only $\sim$125 m above the modern drainage. (2) For a T2 surface that is $<$18.5 ka, the model predicts unreasonably high vertical uplift rates relative to the modern drainage of at least 62 mm/yr. See the online article for the colour version of this figure.

surface at Liuchenzi) likely post-date the Last Glacial Maximum (LGM). The LGM appears to have occurred at ~18.5 ka, as Thompson et al. (1997) argued on the basis of $\delta^{18}O$ data collected from the Guliya ice cap in the Western Kunlun Shan. Two studies <100 km to the east of the Dalong Fault reported strath terrace surface ages and concluded that the majority of the terraces were deposited after the LGM (Van der Woerd et al., 2001; Meriaux et al., 2005). The post-LGM assumption allowed us to evaluate the plausibility of slip rates predicted by the cross-section models we developed.

An important final assumption is that all terrace incision in the hanging wall of the Dalong Fault was driven by tectonism and, in particular, slip along the Dalong Fault, rather than climate change. Although this assumption may seem extreme, it should be emphasized that our analysis is only concerned with tracking local incision of the hanging wall relative to the footwall. In particular, we assume that the drainage responsible for both the formation and subsequent incision of terraces in the hanging wall of the Dalong Fault has (1) maintained a constant gradient through time, consistent with the observation that the abandoned terraces are approximately parallel with the modern drainage (Fig. 6), (2) that the drainage profile can be approximated as a straight line, consistent with the short (~5 km) stream reaches spanned by our model, and (3) that the stream profile has not moved relative to the modern surface of the footwall block, consistent with the observation that no streams are significantly entrenched into the bajada surface to the north of the Dalong Fault. It is our expectation that if some of the hanging wall incision were due to climactic effects, then the footwall reaches of the streams should also be incised. It is also important, however, to consider an alternative possibility that climactic effects could have produced aggradation, rather than incision within the footwall. If the footwall reach of the stream has aggraded, then the surfaces that correlate with the incised terraces in the hanging wall are actually buried at variable depths beneath the bajada surface in the footwall, rather than lying along the modern surface, as we have assumed. In this case, the distance between the top of an abandoned terrace in the hanging wall to the elevation of the modern stream in the footwall underestimates the total vertical component of slip along the fault since the time of abandonment of the hanging wall terrace. It thus follows that if footwall aggradation was significant, then the slip rate computed from our analysis provides only a minimum estimate of the true rate.

We used fault-bend fold, kink-band fault-propagation fold, and trishear fault geometries to match the geometric and kinematic constraints discussed above. In the following, we evaluate both the extent to which each geometric model matches the integrated bedrock and neotectonic data, and explore the kinematic implications of each model. A target for future work will be to conduct more detailed field studies so that additional indicators of kinematic style, such as the geometry of subsurface growth strata, may be used to further test the models.

4.2. Fault-bend fold

Following the approach of Lavé and Avouac (2000) and Thompson et al. (2002), we first assumed a fault-bend fold geometry (Suppe, 1983) at the Liuchenzi site (Fig. 7a). To construct this model, we focused on both the 620-m-wide (horizontal) dip panel in the T2 profile and the 30-m-high fault scarp (Fig. 6). In the fault-bend-fold model, the scarp results from motion of the hanging wall up a south-dipping ramp, and the dip panel results from northward transport of the hanging wall across a bend in the underlying fault. In particular, we assumed that the fault dips more steeply down-dip and to the south of the bend than it does up-dip and to the north, such that the T2–T4 dip panel results from emplacement of a hanging wall section with a steeper cutoff angle against a footwall section with a shallower cutoff (Fig. 7a). By assuming this fault geometry, we were able to use the width of the T2–T4 dip panel and the scarp height to derive the magnitude of total slip post abandonment of T2, the dip of the fault, and the change in fault dip at the bend. In particular, the 620-m-wide T2 dip panel constrains the amount of slip. To produce the 30 m of vertical offset with 620 m of horizontal shortening, requires that the shallowest portion of the underlying fault dips ~3° (fault dip = arctan (30 m/620 m) = 2.95°). To calculate the change in fault dip at the kink, we used the difference (~4°) between the dip of the T2–T4 terraces within the dip panel (7–9°) and their undeformed reaches to the south (3.5–4°) to determine that the underlying fault should also change dip by the same amount. Thus, the dip of the Dalong Fault is predicted to steepen from ~3 to ~7° approximately 1100 m south of the fault scarp.

The lack of terrace deformation south of the southern edge of the 620-m-wide T2–T4 dip panel permits no further down-dip changes in fault dip for a minimum of 3.7 km south of the fault scarp. Thus, a steep fault dip cannot be achieved until ~4 km south of the fault scarp. The orientation of the hanging wall cutoff that defines the anticline gives the orientation of footwall cutoff (28°). Upon cutting down to just below the gn/Tss contact, the model predicts the fault transitions to a décollement.

Although the fault-bend fold solution shown in Fig. 7a satisfies most of the neotectonic and bedrock data, it has four unrealistic implications for the Dalong Fault. First, it predicts the fault dips <10° for over 3.7 km south of the frontal scarp, in contrast to the observed ~50° dip in Zhang and Dalong Valleys (Fig. 5c and d). Second, it predicts a ~6.8-km-long sliver of basement that is only a few hundred meters thick, which is not consistent with the 2 km fault-perpendicular dimensions of the basement exposures seen within the Zhang and Dalong Valleys. Third, if T2 is no older than ~18.5 ka, then the fault-bend fold solution implies a minimum horizontal shortening rate of at least

33.5 mm/yr (620 m horizontal transport/18,500 yrs = 33.5 mm/yr). This rate is unreasonably large considering that the total Indo-Asian convergence rate is only 38–50 mm/yr (DeMets et al., 1990, 1994; Wang et al., 2001). Fourth, the mismatch between the predicted fold-axis location at the gn/Tss contact is nearly 500 m. For these reasons, we concluded that, although fault-bend-fold models work well for regions like the Himalayan front that are characterized by a thin-skinned style of deformation, it fails to explain the basement-involved, thick-skinned, Dalong Fault.

4.3. Kink-band fault-propagation fold

The second model we tested against the Liuchenzi data employed a standard kink-band fault-propagation fold combined with a footwall break-out (Fig. 7b). In this analysis, we followed the geometric analysis of Suppe and Medwedeff (1990). In particular, we used a steeply dipping fault, consistent with previous work in the Qilian Shan and Nan Shan thrust systems (Meyer et al., 1998; Van der Woerd et al., 2001).

To construct this model, we used the bedrock data to constrain fault geometry. Based on our measurements of the forelimb (14°) and backlimb (39°) dip angles, constant-thickness fault-propagation fold theory predicts a 49° fault dip at depth that steps up to a 57° dip (calculated from fig. 22 in Suppe and Medwedeff (1990)). The contacts observed in the field and the stratigraphic thicknesses calculated from these observations, particularly north of the fold axis, were used to generate the bedrock section. The location of the hanging wall fold axis predicted by this model is within 125 m of the predicted gn/Tss fold axis. This model closely approximates the geometry of the observed bedrock data.

To generate the deformation observed in the T2–T4 dip panel, we assumed that the fault that produced the bedrock anticline subsequently broke-out. To calculate the orientation of this break-out, we used the inference from the fault-bend-fold analysis above that an up-dip decrease in fault dip by ~4° is responsible for creating the T2–T4 dip panel. Thus, we assumed that the break-out fault dips 53°. To calculate the position of this break-out, we bisected the southern portion of the dip panel and projected this line until it intersected the fault (Fig. 7b). The depths of the footwall gn/Tss and Tss/Cgl contacts were calculated by assuming 1150 m of vertical slip, which is the amount needed to produce the 620-m-wide dip panel of T2.

As with the fault-bend-fold solution, the kink-band fault-propagation-fold model also makes a number of unreasonable predictions. Because the fault dips steeply, the model requires 1150 m of vertical separation to transport material 620 m in the horizontal direction and form the T2–T4 dip panel. These displacements are not consistent with either the 30-m-high fault scarp or the height of the highest terrace, T4, only ~125 m above the modern drainage. In addition, if the T2 surface is less than 18.5 ka old, then this model predicts it has been uplifted relative to the modern drainage at an unreasonable rate of at least 62 mm/yr (1150 m vertical displacement/18,500 yrs = 62.1 mm/yr). Thus, although a kink-band fault-propagation fold satisfies the bedrock data, it both fails to comply with the terrace-to-modern-drainage height and it predicts an unreasonably high vertical slip rate.

4.4. Trishear fault-propagation

The trishear theory of fault-related folding was first described by Erslev (1991) and has subsequently been expanded upon in a number of studies (Hardy and Ford, 1997; Allmendinger, 1998; Zehnder and Allmendinger, 2000; Allmendinger et al., 2004). According to this theory, slip along a propagating fault is accommodated by distributed strain within a triangular zone of deformation that radiates from the fault tip. We modified the trishear theory by tracking strain recorded by terrace surfaces, in addition to deformation of bedrock. As is shown below, by using trishear kinematic models we were able to satisfy both the geological and neotectonic data at the Liuchenzi and Qingyazi sites.

The trishear fault-propagation model has six parameters: (1) fault dip, (2) X and (3) Y positions of the fault tip, (4) slip, (5) the propagation-to-slip ratio (P/S), and (6) the trishear angle (Allmendinger, 1998, 1999). Dip and the X and Y locations of the fault are usually determined by directly measuring the geometry of the structure from a geologic map or subsurface section. Total slip is usually estimated by reconstructing piercing points. The P/S ratio is simply the ratio of tip propagation to fault slip. The physical properties that control the P/S ratio are not well known, but factors such as lithology, strain rate, and fluid pressure are thought to be important (Allmendinger, 1998). The trishear angle is the angular width of the wedge of distributed strain at the propagating fault tip. The last two variables are more difficult to constrain with field data.

We constructed the trishear models using the computer program Fault/Fold v.5.0 (http://www.geo.cornell.edu/geology/faculty/RWA/RWA.html), which is based on algorithms presented in Allmendinger (1998) and Zehnder and Allmendinger (2000). We began by creating a stratigraphic column of bedrock units overlain by a stream with the same gradient as that measured in the field (Fig. 8). We then propagated a steeply dipping fault from depth and removed all bedrock material in the hanging wall that passed through the stream boundary so as to simulate erosion of the growing fold. When the orientations of the deformed bedrock units approached those measured in the field, we ‘emplaced’ the oldest terrace unit by adding a strain-marker line with the same gradient and position as the stream. Propagation of the fault was then continued so as to uplift and deform this terrace as a passive strain marker relative to the footwall-fixed stream. A second terrace was then emplaced, and propagation of the fault

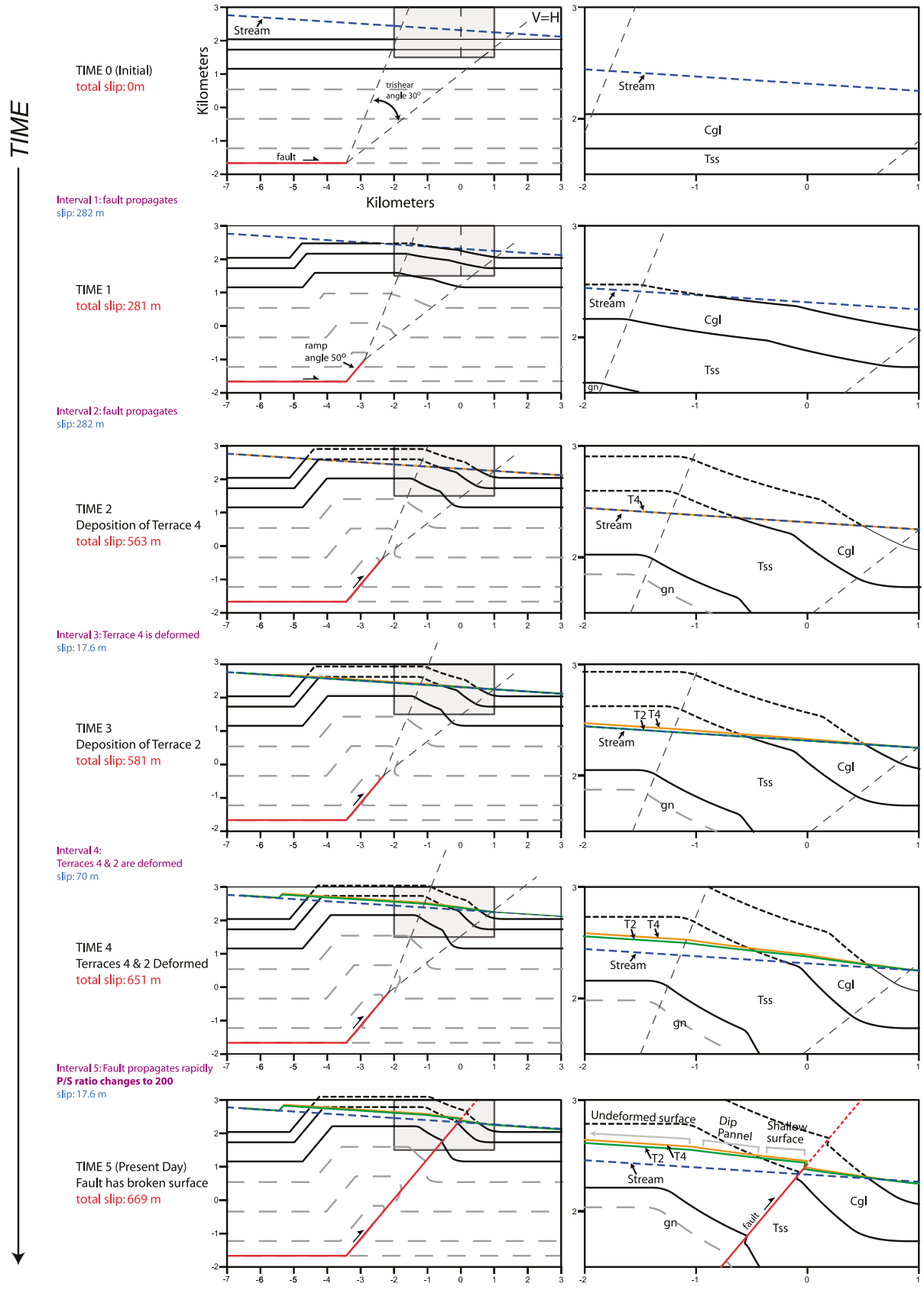

Fig. 8. Evolutionary sequence of the trishear model for the Liuchenzi site. Initial configuration is shown at the top with the final, present-day configuration at the bottom. Left-hand column shows full solution, right-hand side shows enlargement of the fault scarp and terrace topography. Models were constructed using Fault/Fold v.5.0 based on algorithms discussed in Allmendinger (1998) and Zehnder and Allmendinger (2000). The solution shown here was generated using

was continued so as to deform both terraces by uplifting them relative to the stream. To form a fault scarp, we then increased the *P*/*S* ratio so the fault would propagate very rapidly with respect to the increments of slip. The final result was an emergent fault, along which total displacement has produced a strongly deformed bedrock anticline capped by less deformed terraces.

4.4.1. Trishear parameters for the Dalong fault system

For the Dalong fault system, we assumed a fault dip of 50° based on our observations in Zhang Valley and a compilation of fault dips elsewhere in the study area (Fig. 5d). The *X* and *Y* location of the fault tip is therefore constrained to have migrated along a 50° dipping plane that extends down-dip from the fault scarp. To simplify the trishear modeling, we considered only two deformed terraces at the Liuchenzi and Qingyazi sites. We selected the oldest terraces (T4 and Q3) for which we have surface information and also one intermediate terrace level (T2 and Q2) at each locality. Slip was measured by scaling the model to the terrace profiles and calculating a scaling factor between the model output and the fault.

Due to the uncertainty in selecting a *P*/*S* ratio, we used a constant value of 1.5 for the initial stages of deformation in all models. This is an intermediate value in the range of fault-propagation folding. We changed the *P*/*S* value to 200 in the final step of most models to force the fault to propagate very rapidly and create the surface break-out and associated fault scarp. This adjustment reflects the likelihood of the fault propagating very rapidly as it approaches the free boundary at the surface of the earth, thereby forming a break-out (Mitra, 1990; Suppe and Medwedeff, 1990).

Our underlying goal was to see if the trishear model provides a satisfactory fit to the data and to identify the key variables to which the model seems to be most sensitive. Future work will be needed to fully explore parameter space and the sensitivity of the model. It should be noted that the Fault/Fold v.5.0 program does not consider heterogeneous trishear, thus the models derived do not cover all possibilities. Also, the geometry of the terrace surfaces are very difficult to model uniquely, so there is a degree of uncertainty associated with the best-fit models we present below. Factors varied for this investigation were the timing of (1) terrace emplacement and (2) the change in *P*/*S* ratio, as well as (3) the trishear angle. For the Liuchenzi site we tested 14 models and for the Qingyazi site we tested 28. Fig. 9 shows the best-fit model for each site, and model parameters are indicated in Fig. 8.

4.4.2. Trishear model: Liuchenzi

Fig. 9a shows the trishear model for Liuchenzi and matches a number of key bedrock and neotectonic observations. In terms of bedrock data, the positions of the gn–Tss and Tss–Cgl contacts depicted in the model correspond with those observed in the field as measured relative to the fault scarp and indicated in the map shown in Fig. 3b. Likewise, the hanging-wall anticline formed by trishear deformation prior to surface rupture reproduces the bedrock orientations measured in the field. In addition, the model fold hinge along the contact between the basement gneiss (gn) and the siltstone (Tss) is located within ~100 m of the projection of the mapped hinge line into the plane of the section. Lastly, the fault dip used in the model is consistent with orientations observed elsewhere in the Dalong fault system.

In terms of the neotectonic data, the model closely matches the surface deformation of the two modeled terraces. In particular, the 31-m-high fault scarp in the model matches the measured 30-m-high scarp. The model replicates the shallowly dipping terrace surface that extends ~550 m south of the fault scarp. It also reproduces the 620-m-wide T2–T4 dip panel, and the >2.6-km-wide section of undeformed terrace surface to the south. In detail, however, the modeled 'modern' stream profile lies 47 m vertically below the observed stream profile. The stream mismatch may indicate that the stream is in a state of disequilibrium from the most recent series of ruptures and is thus downcutting to resume its original footwall-fixed profile. Alternatively, the mismatch may be due to the relatively large distance over which the stream data are projected into the section (300–1500 m perpendicular to the plane of section). Another possibility is that the mismatch results from an error in the choice of model parameters, such as the stream elevation relative to the nucleation site of the propagating fault. An additional concern is that the Dalong Fault may have a shallow dip where it crosses the line of section, as indicated by the southward embayment of the fault scarp in this area. However, as is shown above in the discussion of the fault-bend fold model, such a shallowly dipping fault cannot be reconciled with a number of other field observations. Alternative explanations for the embayment are that it reflects a non-planar fault geometry (e.g. Axen et al., 1999) or near-surface reduction of the fault dip

the following model parameters and increments: model begins with stratigraphic column and minimum detachment depth for fault of −1.5 km below mean sea level; fault dip, 50°; trishear angle, 30°; and initial *P*/*S* ratio, 1.5. Interval 1: fault slips 282 m and propagates up ramp; deform bedrock to form anticline. Time 1: erode all bedrock that lies above stream horizon; total slip is 282 m. Interval 2: slip 281 m; deform bedrock as in interval 1. Time 2: erode bedrock as above; form T4 surface; total slip is now 563 m. Interval 3: slip 17.6 m; deform T4 and bedrock. Time 3: locally erode T4 along the drainage to form T2 as inset terrace; total slip is now 581 m. Interval 4: slip 70 m; deform T2, T4, and bedrock. Time 4: locally erode T2 along drainage to form younger terraces; total slip is now 651 m. Interval 5: change *P*/*S* ratio to 200, slip 17.6 m, fault propagates rapidly to the surface to form break-out. Time 5 (present day): locally erode hanging wall so stream will return to the footwall-fixed reference level; total slip is 669 m. See the online article for the colour version of this figure.

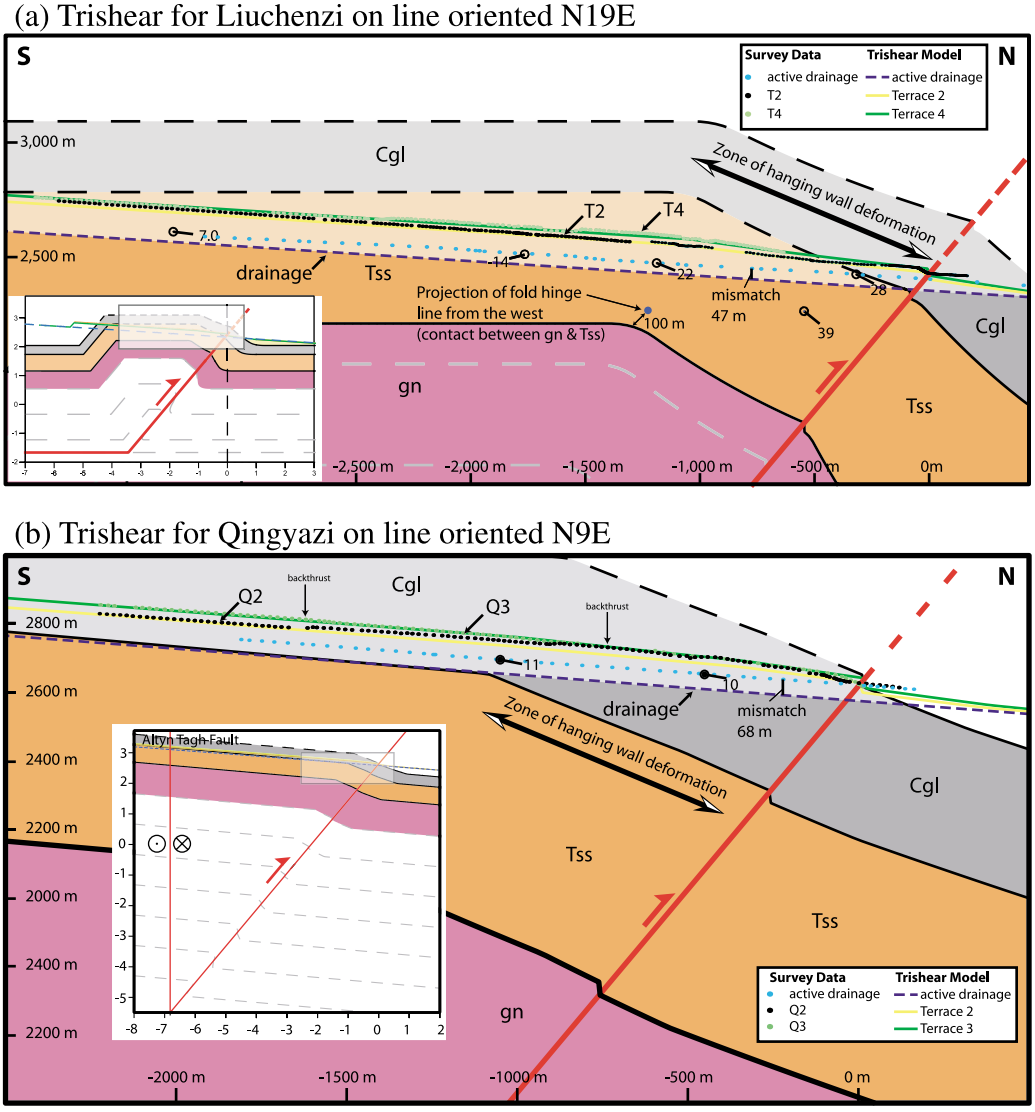

Fig. 9. Final trishear solutions compared with field data for (a) Liuchenzi and (b) Qingyazi. Insets show full model solution. Modeled bedrock deformation is shown with solid colors. Modeled terraces are shown as solid lines. Bedrock measurements made in the field and projected into the line of section are shown as dip ticks. Surface measurements of the terraces (T2–T4 and Q2–Q3) as well as the modern drainage are shown as green dots. The model parameters and increments for the Liuchenzi model are described in the caption to Fig. 8. The model parameters for Qingyazi are as follows: detachment depth for fault of −5.5 km below mean sea level; fault dip, 50°; trishear angle, 10°; and initial *P*/*S* ratio, 1.5. Interval 1: slip 506 m, deform bedrock. Time 1: erode bedrock and deposit Q3; total slip is 506 m. Interval 2: slip 31.6 m to deform Q3 and bedrock. Time 2: locally erode bedrock and Q3 to form Q2; total slip is 537.2 m. Interval 3: slip 31.6 m to deform Q3, Q2, and bedrock. Time 3: locally erode Q3; total slip is 568.8 m. Interval 4: change the *P*/*S* ratio to 200 and slip 63.2 m to rapidly propagate the fault to the surface and form the break-out. Time 4 (present day): locally erode hanging wall so stream will return to the footwall-fixed reference level; total slip is 632 m. See the online article for the colour version of this figure.

within a few hundred meters of the fault scarp (e.g. Arrowsmith and Strecker, 1999).

4.4.3. Trishear model: Qingyazi

At Qingyazi, the trishear model (Fig. 9b) matches the bedrock record. Principally, it conforms to the low magnitude deformation observed in the Cgl unit (<15° dips near the fault rupture) and is also consistent with the observation that no deeper structural levels are exposed. A lack of footwall data and deeper structural data makes the remaining cover and bedrock model predictions difficult to evaluate.

We modeled the Q2 and Q3 surfaces (Fig. 9b) and found that the trishear model agrees with several aspects of the neotectonic data. First, the upper modeled terrace surface replicates the Q3 surface data. Second, the spacing between Q2 and Q3 is accurately modeled >1500 m from the frontal scarp. There are two primary mismatches between the model and the measured terrace surfaces. First, the model terrace does not match the measured Q2 profile for ~1620 m, between the Dalong Fault in the north and the second backthrust in the south. We interpret this mismatch to result from slip along the two backthrusts (Fig. 6) that has elevated the Q2 surface relative to that

farther upstream. This local deformation is not accounted for by the model. Another possible explanation is the large distance (>500 m) over which the Q2 data was projected into the section. The second mismatch is similar to that observed at the Liuchenzi site, where the modeled drainage lies ~68 m below the measured active drainage. As with Liuchenzi, this problem could reflect distortion from data projection in the section (300–1500 m perpendicular to the plane of section), disequilibrium in the present-day stream profile from the most recent fault rupture, or an error in the choice of model parameters.

Despite these mismatches, the trishear model matches the first-order bedrock and neotectonic observations for both the Qingyazi and Liuchenzi areas along the Dalong reverse fault. The trishear model also makes geologically reasonable predictions regarding the slip rate along the Dalong Fault at both sites. Unlike the unreasonably high slip rates predicted by the fault-bend and fault-propagation fold models, the trishear model predicts minimum slip rates of 5.7 mm/yr for Liuchenzi and 6.4 mm/yr for Qingyazi if the upper terrace surface (T4 and Q3, respectively) postdate the LGM (<18.5 ka). These values closely match slip rates reported along the Tanghe Nan Shan at its intersection with the Altyn Tagh Fault (Van der Woerd et al., 2001).

5. Implications

5.1. Near-field deformation

The trishear model presented above has important implications for studies that use dated terraces to infer fault slip rates. In particular, the trishear model predicts a zone of distributed deformation above the active fault, which, for the Liuchenzi and Qingyazi sites, extends into the hanging wall for over a kilometer from the emergent fault scarp (Fig. 9). Clearly, if vertical offsets are measured across the frontal fault scarp but do not extend outside of this broad zone of deformation, erroneously low slip rates will be determined.

Fig. 10 schematically illustrates the significance of this near-field zone of deformation. In this example, a fault at depth generates a zone of distributed deformation in an overlying terrace and then propagates to the surface. A small

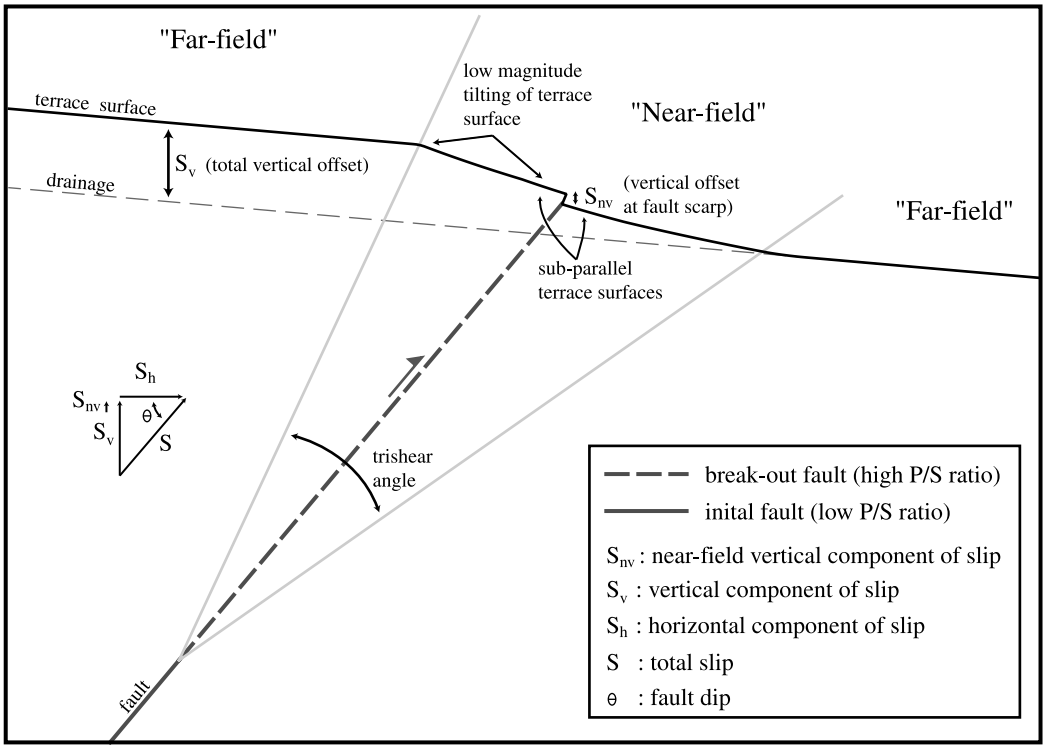

Fig. 10. Schematic illustration of deformation associated with trishear fault-propagation folding. In this example, a terrace surface is both folded and faulted during two stages of deformation. In the first stage, the *P*/*S* ratio is low (<15), producing near-field tilting inside the trishear wedge. If the wedge angle is large, only small tilt angles are produced by large total slip (i.e. large S_v values). In the second stage, the fault breaks through the trishear wedge. The final result of this scenario is a zone of deformation that is divided into two components: near-field and far-field. In the zone of near-field deformation, a terrace surface accommodates strain through tilting and faulting. The terrace surfaces in the hanging wall and footwall in close proximity to the fault scarp may have near-parallel dips, but measurement of the vertical offset at the fault will only record a sub-component (S_{nv}) of the total component of vertical slip (S_v). In the far-field zone, the terrace surfaces are parallel in the hanging wall and footwall and measurement of the total vertical separation between these surfaces yields the full component of vertical slip (S_v). The width of the near-field strain zone is a function of the depth of the fault tip and the width of trishear angle. The magnitude of terrace tilting is a function of both the *P*/*S* ratio and trishear angle. In this example, the fault dips 50° and has a trishear angle of 30°.

scarp is formed at the location where the fault breaks the surface, but a local measurement at the fault scarp does not capture the full strain field recorded by the terrace. Instead, the vertical offset between the terrace hanging wall and footwall surfaces must be measured a great distance from the fault scarp (as much as a factor of 35 times greater than the vertical height of the T2 fault scarp at the Liuchenzi site). In the far-field, outside of the zone of distributed deformation, the hanging wall terrace surfaces should be parallel both with the footwall terrace and with the modern drainage.

An important aspect of this near-field deformation field is that the record of this distributed strain zone is only a small angular tilt in the terrace surface within the trishear wedge (Fig. 10). In the case of the Liuchenzi site, this angular tilt only reaches a maximum of ~9° for the oldest, T4 surface (Fig. 6), which could be easily interpreted to record the original inclination of the depositional surface. Thus, faults may produce wide zones of strain that give small angular terrace tilts inside the wedge, but actually reflect very large total slip along the underlying fault. Furthermore, if the propagating fault roughly bisects the trishear wedge as it breaks out, the terrace slope angles will match on either side of the fault scarp inside the wedge. The uniformity of terrace slopes above and below the scarp has been used in some studies to argue that measured topographic profiles have captured the total displacement field, but as Fig. 10 indicates, this will be an erroneous conclusion if the profiles do not extend outside the wedge. This problem is particularly well illustrated at the Liuchenzi site, where the T2 surface dips ~3.5° in both the hanging wall and footwall adjacent to the fault scarp but still lies within an inferred trishear wedge (Fig. 6).

Ultimately, the width of this zone of distributed strain is a function of the trishear angle and the depth of the fault tip. Faults with wide trishear angles and greater depth will produce wider zones of distributed deformation than faults with narrow trishear angles and shallow depths. Moreover, the magnitude of terrace deformation (tilting) within the wedge will be a result of both the trishear angle and the *P*/*S* ratio, although it is far more sensitive to the *P*/*S* ratio, as demonstrated by Allmendinger (1999) and Allmendinger et al. (2004).

To illustrate the importance of this zone of distributed deformation, consider the example of the T2 surface at the Liuchenzi site, which is cut by the Dalong Fault to form a ~30-m-high fault scarp. If the age of the T2 surface were known, a typical method for calculating an uplift rate on this fault would be to divide the vertical offset (30 m) by the measured age of the surface. For example, if the T2 surface was dated at 10 ka, then the vertical slip rate would be calculated at 3 mm/yr. However, a closer examination shows that at a distance of 1100 m south of the scarp, the T2 surface is perched 84 m above the modern drainage (Fig. 6), which we think is due to distributed deformation within the hanging wall of the Dalong Fault. Under the assumption that the longitudinal profile of the drainage has maintained a constant shape and position relative to footwall since T2 formed, then the 84 m height of T2 reflects the amount of vertical displacement since the T2 terrace was abandoned. If we again assume this abandonment occurred at 10 ka, then the true uplift rate is 8.4 mm/yr, or almost three times higher than the rate calculated from the fault scarp alone. Thus, trishear modeling provides a method to understand the near-field zone of distributed deformation, within which, measurements of vertical offsets will result in anomalously low slip rates.

The above analysis raises an important question regarding the ability of trishear theory to accurately model strain associated with fault slip. A simplifying assumption of the trishear model is that the shear wedge is tied to the fault tip. Thus, to produce both the far-field strain zone and the near-field fault scarp we have used a two-stage sequence of early trishear followed by fault breakout. But what if strain within the trishear wedge is heterogeneous? In this case, both trishear and fault breakout may occur simultaneously, such that the wedge continues to deform internally even after the fault (or shear zone) has propagated through it. In this case, total slip at depth produces both surface displacement along the emergent fault scarp and distributed surface deformation that is spread across the trishear wedge. Testing this hypothesis of heterogeneous strain is important because the potential implications of this more complex scenario are significant for paleoseismological studies: the total slip for a single thrust event that is observed within a trench that only spans the emergent scarp will underestimate the total slip at depth. Thus, small displacements observed in trench logs may in fact reflect large earthquakes.

In summary, our analysis has several important implications for neotectonic studies. First, a wedge of distributed surface deformation may exist above a propagating fault tip. The width of this wedge is a function of the depth of the fault and trishear angle. Second, the distributed strain field will be expressed as angular tilting of terrace surfaces, the magnitude of which is controlled by the trishear angle and the *P*/*S* ratio. The degree of tilting within this wedge can be very subtle, thus care must be taken when measuring displaced and deformed geomorphic markers to ensure that the total, far-field gradient (i.e. sum of a local fault scarp and near-field strain recorded by terrace tilting) is accounted for. Third, warning signs that distributed deformation may need to be accounted for include terraces that gradually diverge upstream but then become parallel to one another, and scarp profiles that do not have the same gradients in the hanging wall and footwall adjacent to an emergent fault scarp. Finally, our analysis leads to the following provocative, but unsettling question: what if distributed deformation along emergent faults produces scarp ruptures that significantly under-record the total slip at depth and therefore the true size of the earthquake?

6. Conclusions

We have shown that where conventional fault-bend folding and kink-band fault-propagation folding kinematic models fail, trishear fault-propagation folding offers a promising mechanism for modeling deformation in the bedrock and neotectonic record within the steeply-dipping, basement involved Dalong fault system. An important implication from this work is the identification of a wide zone of surface deformation adjacent to the active fault scarp. In the cases examined here, the zone extends over 1 km into the hanging wall from the emergent fault. To calculate accurate vertical incision and tectonic uplift rates, terrace heights must be measured outside this zone of distributed deformation.

To our knowledge, this is the first study that fully integrates bedrock and neotectonic observations to derive kinematic models for steeply-dipping, basement involved faults. Our model provides precise constraints on subsurface fault geometry and fault kinematics and lays the foundation for making robust slip-rate calculations. It also provides a link between deformation at Quaternary timescales, which is necessary for evaluating the timescale over which recently-proposed secular variation in fault slip rates may occur. Future investigations will evaluate whether trishear-fault propagation can be extended to link deformation in the bedrock and neotectonic records of other reverse fault systems and also test the match between observed subsurface growth strata geometry and the geometries predicted by the trishear model. Additionally, future work is required to evaluate if trishear continues to deform local material internally, even after the fault has propagated through it. This type of internal deformation may have important implications for paleoseismological studies because near-field deformation outside of the scarp rupture may not be accounted for. Thus, trench-based studies may not capture the total slip per event and therefore the true size of the past earthquakes.

Acknowledgements

We thank Guo Anan and the Institute of Geomechanics in the Chinese Academy of Geological Sciences for logistical support. We are indebted to Christopher Flower for his help with field data collection and also to Richard Allmendinger for making Fault/Fold v.5.0 available. We thank Ramon Arrowsmith for the use of his Corona imagery. Ling Yanxia, Zhang Songlin, Yiang Jialai, and Hui Xu provided outstanding transportation services. We thank Richard Allmendinger and Eric Erslev for their very helpful and constructive reviews. This work benefited from thoughtful discussions with, and reviews by, John Dewey, Sean Mulcahy, Nicholas Raterman, and Todd Ehlers. Ryan Gold's research was conducted with the support of a UC Davis Graduate Research Grant, the UC Davis Department of Geology Durrell funds, and an AAPG grants-in-aid fellowship (Peter W. Gester Memorial Grant). Eric Cowgill acknowledges support by NASA (No. EOS/03-0663-0306). Wang Xiao-Feng and Chen Xuan-Hua acknowledge support by the Major State Basic Research Program of People's Republic of China (No. 2001CB71100103).

Appendix. Terrace descriptions at the Liuchenzi site

At the Liuchenzi site, the highest and oldest terrace unit, T4, is the second-most extensive unit in the area (Fig. 3). It is a 15–20-m-thick strath terrace, cut into the Tss and gn units. It extends from the gn exposures in the south to within 500 m of the Dalong Fault trace in the north. The terrace tread typically lies ~125 m above the active drainage. It is preserved only in the hanging wall of the fault. T4 has the thickest loess cover of any strath terraces in the Liuchenzi valley (20–30 cm) and has the lowest surface clast density of the terraces in the region (average clast diameter is ~4 cm). There is no preservation of channel-and-bar topography on this surface. T4 is the most deeply-incised of the terraces in the Liuchenzi area. In some locations, the terrace has been completely eroded, exposing the underlying redbed unit.

T3 is restricted to the northeastern Liuchenzi area. The tread of this 10-m-thick strath terrace lies ~110 m above the active drainage. The terrace is preserved for only ~250 m in the north–south direction. It is more extensively preserved up-valley (south) where it is characterized by patches of desert pavement that are separated by gullies. Down-valley (north), the terrace deposits are reduced to a knife ridge with no preservation of the tread surface. Surface clast concentration is higher than on T4 and the average clast diameter is ~5–6 cm, with the largest clasts reaching ~50 cm. Like T4, there is no preservation of paleo channel-and-bar surface topography. Also like T4, T3 has a relatively thick cover of loess (20–25 cm) beneath a desert pavement of clasts. The degree of incision of T3 is intermediate between T4 and the less incised lower terrace units.

The T2 surface lies ~85 m above the active drainage and forms the most extensive unit in the Liuchenzi Valley. The terrace deposits are 10–15 m thick. The unit is most widespread along the east side of the Liuchenzi drainage and extends for ~4 km from the Dalong Fault in the north to the basement ridge in the south (Fig. 5a). T2 is cut by a 30-m-high scarp along the Dalong Fault (Fig. 5b). In the footwall of the Dalong Fault, the unit is also preserved (Figs. 3 and 5b). Clast concentrations are greater on the T2 surface than on either T3 or T4, with clast diameters typically 3–4 cm. The largest clasts approach 75 cm in diameter. A desert pavement has formed on this surface, below which there is approximately 10 cm of loess. Below the loess, clasts range in size from millimeter size to 50 cm and are stratified in a matrix of silty sand. The unit is moderately

incised, though less-so than the higher terraces. Muted channel-and-bar topography is preserved on this surface.

The lowest abandoned terrace unit, T1, is a strath terrace, cut into the Tss unit. It lies ~40 m above the active channel and is preserved primarily to the west of the Liuchenzi drainage. The unit is 5–10 m thick and is composed of sand, gravel, and small cobbles. T1 is only preserved in the hanging wall of the Dalong Fault, terminating against the fault at its northernmost extent. A desert pavement has formed on the surface of T1, with the highest clast density observed on the abandoned terrace surfaces. Most clasts on the surface are ~5 cm in diameter, with the largest clasts ranging from 30 to 75 cm. The unit is the least extensively incised of the abandoned terrace surfaces, and the depositional surface is the most youthful, with preserved channel-and-bar topography.

The active depositional surface forms three subunits, which, from old to young, are T0″, T0′, and T0. These units lay ~3–5 m above the active drainage, are primarily preserved in the footwall of the Dalong Fault, and are not cut by the fault system. These surfaces have little loess cover and high preservation of channel-and-bar topography.

References

Allmendinger, R.W., 1998. Inverse and forward numerical modeling of trishear fault-propagation folds. Tectonics 17 (4), 640–656.

Allmendinger, R.W., 1999. Propagation-to-slip ratio and fold style in fault-propagation folds: perspectives gleaned from trishear modeling. Geological Society of America Abstracts with Programs 31 (7), 237.

Allmendinger, R.W., Zapata, T., Manceda, R., Dzelalija, F., 2004. Trishear kinematic modeling of structures, with examples from the Neuquen Basin, Argentina. In: McClay, K.R. (Ed.), Thrust Tectonics and Hydrocarbon Systems. AAPG Memoir 82, pp. 356–371.

Anderson, G., Aagaard, B., Hudnut, K., 2003. Fault interactions and large complex earthquakes in the Los Angeles area. Science 302 (5652), 1946–1949.

Arrowsmith, J.R., Strecker, M.R., 1999. Seismotectonic range-front segmentation and mountain-belt growth in the Pamir-Alai region, Kyrgyzstan (India–Eurasia collision zone). Geological Society of America Bulletin 111 (11), 1665–1683.

Avouac, J.P., 1993. Analysis of scarp profiles: evaluation of errors in morphologic dating. Journal of Geophysical Research 98 (B4), 6745–6754.

Avouac, J.P., Peltzer, G., 1993. Active tectonics in southern Xinjiang, China: analysis of terrace riser and normal fault scarp degradation along the Hotan–Qira fault system. Journal of Geophysical Research 98 (B12), 21,773–21,807.

Axen, G.J., Fletcher, J.M., Cowgill, E., Murphy, M., Kapp, P., MacMillan, I., Ramos-Velázquez, E., Aranda-Gómez, J., 1999. Range-front fault scarps of the Sierra El Mayor, Baja California: formed above an active low-angle normal fault? Geology 27 (3), 247–250.

Benedetti, L., Tapponnier, P., King, G., 2000. Growth folding and active thrusting in the Montello region, Veneto, northern Italy. Journal of Geophysical Research, B, Solid Earth and Planets 105 (1), 739–766.

Burbank, D.A. & Anderson, R.S. 2001. Tectonic Geomorphology. Blackwell Science, Federal Republic of Germany.

Chen, Z., Burchfiel, B.C., Liu, Y., King, R.W., Royden, L.H., Tang, W., Wang, E., Zhao, J., Zhang, X., 2000. Global positioning system measurements from eastern Tibet and their implications for India/Eurasia intercontinental deformation. Journal of Geophysical Research 105 (7), 16,215–16,227.

Chevalier, M.-L., Ryerson, F.J., Tapponnier, P., Finkel, R., Van der Woerd, J., Haibing, L., Qing, L., 2005. Slip-rate measurements on the Karakorum fault may imply secular variations in fault motion. Science 307 (5708), 411–414.

Chinese State Bureau of Seismology, 1992.Anon., 1992. The Altyn Tagh Active Fault System. Seismology Publishing House, Beijing, China (in Chinese with English abstract).

Cowgill, E., Gold, R., Wang, X.-f., Chen, X., 2004a. Strike-slip duplexing and associated fault "roughening": an example from the Aksai restraining stepover along the Altyn Tagh fault, NW China, Abstracts with Programs. Abstracts with Programs 36. Geological Society of America, Denver. 252pp.

Cowgill, E., Yin, A., Arrowsmith, J.R., Xiaofeng, W., Shuanghong, Z., 2004b. The Akato Tagh bend along the Altyn Tagh fault, NW Tibet. Cenozoic structure, smoothing by vertical-axis rotation, and the effect of topographic stresses on borderland faulting. GSA Bulletin 116 (11/12), 1423–1442.

Delville, N., Arnaud, N., Montel, J.-M., Roger, F., Brunel, M., Tapponnier, P., Sobel, E., 2001. Paleozoic to Cenozoic deformation along the Altyn Tagh fault in the Altun Shan massif area, eastern Qilian Shan, northeastern Tibet, China. In: Hendrix, M.S., Davis, G.A. (Eds.), Paleozoic and Mesozoic Tectonic Evolution of Central and Eastern Asia: From Continental Assembly to Intracontinental Deformation. Geological Society of America Memoir 194, Boulder, CO, pp. 269–292.

DeMets, C., Gordon, R.G., Argus, D.F., Stein, S., 1990. Current plate motions. Geophysical Journal International 101 (2), 425–478.

DeMets, C., Gordon, R.G., Argus, D.F., Stein, S., 1994. Effect of recent revisions to the geomagnetic reversal time scale on estimates of current plate motions. Geophysical Research Letters 21 (20), 2191–2194.

Erslev, E.S., 1991. Trishear fault-propagation folding. Geology 19, 617–620.

Friedrich, A.M., Wernicke, B.P., Niemi, N.A., Bennett, R.A., Davis, J.L., 2003. Comparison of geodetic and geologic data from the Wasatch region, Utah, and implications for the spectral character of Earth deformation at periods of 10 to 10 million years. Journal of Geophysical Research, B, Solid Earth and Planets 108 (B4), 23.

GBG, 1977. Geologic map of the Duobagou sheet (J-46-IV) at a scale of 1: 200,000. Ministry of Geology, P.R. of China, Beijing.

Gilder, S., Chen, Y., Sen, S., 2001. Oligo-Miocene magnetostratigraphy and rock magnetism of the Xishuigou section, Subei (Gansu Province, western China) and implications for shallow inclinations in central Asia. Journal of Geophysical Research 106 (12), 30,505–30,521.

Hardy, S., Ford, M., 1997. Numerical modeling of trishear fault propagation folding. Tectonics 16 (5), 841–854.

Jolivet, M., Brunel, M., Seward, D., Xu, Z., Yang, J., Roger, F., Tapponnier, P., Malavieille, J., Arnaud, N., Wu, C., 2001. Mesozoic and Cenozoic tectonics of the northern edge of the Tibetan Plateau; fission-track constraints. Tectonophysics 34, 111–134.

Lavé, J., Avouac, J.P., 2000. Active folding of fluvial terraces across the Siwaliks Hills. Himalayas of central Nepal. Journal of Geophysical Research 105 (B3), 5735–5770.

Manaker, D.M., Andrew, M.J., Burgmann, R., 2005. Subsurface structure and kinematics of the Calaveras–Hayward Fault stepover from three-dimensional Vp and seismicity, San Francisco Bay Region, California. Bulletin of the Seismological Society of America 95 (2), 446–470.

Matmon, A., Schwartz, D.P., Finkel, R., Clemmens, S., Hanks, T.C., 2005. Dating offset fans along the Mojave section of the San Andreas Fault using cosmogenic ^{26}Al and ^{10}Be. Geological Society of America Bulletin 117 (5/6), 795–807.

Meriaux, A.-S., Ryerson, F.J., Tapponnier, P., Van der Woerd, J., Finkel, R., Xiwei, X., Xiwei, X., Caffee, M., 2004. Rapid slip along the central Altyn Tagh Fault: morphochronologic evidence from Cherchen He and Sulamu Tagh. Journal of Geophysical Research, B, Solid Earth and Planets 109 (B6), 1–23.

Meriaux, A., Tapponnier, P., Ryerson, F.J., Xiwei, X., King, G., Van der Woerd, J., Finkel, R., Haibing, L., Caffee, M., Zhiqin, X., Wenbin, C., 2005. The Aksay segment of the northern Altyn Tagh fault: tectonic geomorphology, landscape evolution, and Holocene slip rate. Journal of Geophysical Research, B, Solid Earth and Planets 110 (B4), 1–32.

Meyer, B., Tapponnier, P., Bourjot, L., Metivier, F., Gaudemer, Y., Peltzer, G., Guo, S., Chen, Z., 1998. Crustal thickening in Gansu–Qinghai, lithospheric mantle subduction, and oblique, strike-slip controlled growth of the Tibet plateau. Geophysical Journal International 135, 1–47.

Mitra, S., 1990. Fault-propagation folds: geometry, kinematic evolution, and hydrocarbon traps. The American Association of Petroleum Geologists Bulletin 74 (6), 921–945.

Molnar, P., Tapponnier, P., 1975. Cenozoic tectonics of Asia; effects of a continental collision. Science 189 (4201), 419–426.

Molnar, P., Tapponnier, P., 1978. Active tectonics of Tibet. Journal of Geophysical Research, A, Space Physics 83 (B11), 5361–5375.

Molnar, P., Brown, E.T., Burchfiel, B.C., Qidong, D., Xianyue, F., Jun, L., Raisbeck, G.M., Jianbang, S., Zhangming, W., Yiou, F., Huichuan, Y., 1994. Quaternary climate changes and the formation of river terraces across growing anticlines on the north flank of the Tien Shan, China. Journal of Geology 102, 583–602.

Peltzer, G., Tapponnier, P., 1988. Formation and evolution of strike-slip faults, rifts, and basins during the India-Asia collision; an experimental approach. Journal of Geophysical Research, B, Solid Earth and Planets 93 (12), 15,085–15,117.

Ritz, J.-F., Bourlés, D.L., Brown, E.T., Carretier, S., Chéry, J., Enhtuvshin, B., Galsan, P., Finkel, R., Hanks, T.C., Kendrick, K.J., Philip, H., Raisbeck, G.M., Schlupp, A., Schwartz, D.P., Yiou, F., 2003. Late Pleistocene to Holocene slip rates for the Gurvan Bulag thrust fault (Gobi-Altay, Mongolia) estimated with ^{10}Be dates. Journal of Geophysical Research, B, Solid Earth and Planets 108 (3), 2161–2177.

Rubin, C.M., Lindvall, S.C., Rockwell, T.K., 1998. Evidence for large earthquakes in metropolitan Los Angeles. Science 281 (5375), 398–402.

Suppe, J., 1983. Geometry and kinematics of fault-bend folding. American Journal of Science 283, 684–721.

Suppe, J., Medwedeff, D.A., 1990. Geometry and kinematics of fault-propagation folding. Eclogae Geologicae Helvetiae 83 (3), 409–454.

Tapponnier, P., Molnar, P., 1977. Active faulting and tectonics in China. Journal of Geophysical Research 82 (20), 2905–2930.

Thompson, L.G., Yao, T., Davis, M.E., Henderson, K., Mosley-Thompson, E., Lin, P.-N., J, L., Beer, J., Synal, H.-A., Cole-Dai, J., Bolzan, J.F., 1997. Tropical climate instability: the last glacial cycle from a Qinghai–Tibetan ice core. Science 276, 1821–1825.

Thompson, S., Weldon, R., Rubin, C., Abdrakhmatov, K., Molnar, P., Berger, G., 2002. Late Quaternary slip rates across the central Tien Shan, Kyrgyzstan, central Asia. Journal of Geophysical Research, B, Solid Earth and Planets 107 (9), 1–32.

Van der Woerd, J., Xu, X., Li, H., Tapponnier, P., Meyer, B., Ryerson, F.J., Meriaux, A.-S., Xu, Z., 2001. Rapid active thrusting along the northwestern rangefront of the Tanghe Nan Shan (western Gansu, China). Journal of Geophysical Research 106 (B12), 30,475–30,504.

Vannoli, P., Basili, R., Valensise, G., 2004. New geomorphic evidence for anticlinal growth driven by blind-thrust faulting along the northern Marche coastal belt (central Italy). Journal of Seismology 8 (3), 297–312.

Wang, E., 1997. Displacement and timing along the northern strand of the Altyn Tagh fault zone, Northern Tibet. Earth and Planetary Science Letters 150, 55–64.

Wang, Q., Zhang, P.-Z., Freymueller, J., Bilham, R., Larson, K.M., Lai, X.a., You, X., Niu, Z., Wu, J., Li, Y., Liu, J., Yang, Z., Chen, Q., 2001. Present-day crustal deformation in China constrained by global positioning system measurements. Science 294, 574–577.

Wang, X., Wang, B., Qiu, Z., Xie, G., Xie, J., Will, D., Qiu, Z., Deng, T., 2003. Danghe area (western Gansu, China) biostratigraphy and implications for depositional history and tectonics of northern Tibetan Plateau. Earth and Planetary Science Letters 208 (3–4), 253–569.

Washburn, Z., Arrowsmith, J.R., Forman, S.L., Cowgill, E., Wang, X., Zhang, Y., Chen, Z., 2001. Late Holocene earthquake history of the central Altyn Tagh Fault, China. Geology 29 (11), 1051–1054.

Weldon, R., 1986. The late Cenozoic geology of Cajon Pass; implications for tectonics and sedimentation along the San Andreas Fault. Ph.D. Thesis. California Institute of Technology, Pasadena.

Weldon, R., Sieh, K., 1985. Holocene rate of slip and tentative recurrence interval for large earthquakes on the San Andreas fault, Cajon Pass, southern California. Geological Society of America Bulletin 96 (6), 793–812.

Weldon, R., Scharer, K., Fumal, T., Biasi, G., 2004. Wrightwood and the earthquake cycle; what a long recurrence record tells us about how faults work. GSA Today 14 (9), 4–10.

Xu, X., Deng, Q., 1996. Nonlinear characteristics of paleoseismicity in China. Journal of Geophysical Research, B, Solid Earth and Planets 101 (3), 6209–6231.

Yeats, R.S., Prentice, C.S., 1996. Introduction to special section: paleoseismology. Journal of Geophysical Research, B, Solid Earth and Planets 101 (3), 5847–5853.

Yin, A., Harrison, T.M., 2000. Geologic evolution of the Himalayan–Tibetan orogen. Annual Review of Earth and Planetary Science 28, 211–280.

Yin, A., Rumelhart, P.E., Butler, R., Cowgill, E., Harrison, T.M., Foster, D.A., Ingersoll, R.V., Zhang, Q., Zhou, X., Wang, X., Hanson, A., Raza, A., 2002. Tectonic history of the Altyn Tagh fault system in northern Tibet inferred from Cenozoic sedimentation. Geological Society of America Bulletin 114 (10), 1257–1295.

Zehnder, A.T., Allmendinger, R.W., 2000. Velocity field for the trishear model. Journal of Structural Geology 22 (8), 1009–1014.